Arab American University

Faculty of Graduate Studies

Iron doping effects on Bi_2O_3 optical filters

By

Samah Sameer Abd Atari

Supervisor

Prof. Dr. Atef Fayez Qasrawi

This thesis was submitted in partial fulfillment of the requirements for the Master's degree in Physics

April /2024

Thesis Approval

Iron doping effects on Bi_2O_3 optical filters

By

Samah Sameer Abd Atari

This thesis was defended successfully on April 25th 2024 and approved by:

Committee members	Signature
1. Prof. Dr. Atef Fayez Qasrawi: Supervisor	
2. Prof. Dr. Hazem Khanfar: Internal examiner	
3. Assoc. Prof. Dr. Iyad Saadeddin: External examiner	

Declaration

The work in this thesis, unless otherwise referenced, is the researcher's own work and has not been submitted elsewhere for any other degree or qualification.

Student's Name: Samah Sameer Abd Atari

Student ID: 202120190

Signature: Samah Atari

Date: 25.07.2024

Acknowledgments

All thanks to Allah who enabled me to overcome difficulties and gave me strength and patience to complete this thesis successfully.

I dedicate this thesis to my great supervisor, Prof. Dr. Atef Qasrawi, who provided me with advice and guidance during my study. I am very grateful to him because he gave me a lot of his knowledge, he was always ready to answer my inquiries and questions and gave me the opportunity to conduct all the experiments that would enable me to develop my thesis. His exceptional insight and broad view led me to wonderful work in the scientific research lab. I am so proud of him for being my supervisor.

Special thanks to the kind assistant Rana Daraghmeh, who walked with me step by step from the first day of working on the experiments until this day, the day I write my thesis. I ask Allah to reward her with the best reward.

At the end, I offer my gratitude to my family, parents, brothers and sister for their unconditional love and support during all stages of my study life.

Abstract

In this thesis, we have discussed the effects of iron doping on the structural, morphological, compositional, optical and dielectric properties of bismuth oxide thin films. Bismuth oxide thin films of thicknesses of $0.50\ \mu m$ were deposited by the thermal evaporation of Bi_2O_3 powders onto glass substrates under a vacuum pressure of $\sim 10^{-4}$ mbar. Iron doping into the films was actualized by mixing the iron nanopowders with those of Bi_2O_3 before evaporation. Three increasable doping contents were used for this purpose. It was observed that the grown films are polycrystalline in nature. The doping strongly affected the crystallinity, as evidenced from the decreased crystallite sizes and increased micro-strains and defect densities upon doping. However, increasing the doping content showed less effect on the structural parameters even after the solubility limit of iron was exceeded ($FBO-13$). The behavior is ascribed to the formation of iron oxide in the structure of bismuth oxide. The scanning electron microscopy showed grains with increasing sizes and different shapes based on the doping amount. Optically, the films showed low transmittance values and exhibited a red shift in the energy band gap with increasing doping content. On the other hand, the dielectric dispersion analyses have shown a well improved dielectric response suiting high k-gate dielectrics that are used in thin film transistor technology. The Drude-Lorentz model analysis that connects electrical parameters to those corresponding optical ones was fitted with the experimental data showing decreasing carrier density with increasing doping content. The doping showed no effect on the drift mobility or other related conduction parameters other than the Plasmon frequency, which decreased with increasing doping content. The work is promising as it enhances the performance of Bi_2O_3 and makes it adequate for electronic applications in isolation purposes.

List of Contents

List of Tables

List of Figures

List of Symbols

Symbol	Symbol Meaning
Bi_2O_3	Bismuth oxide
MOs	Metal oxides
M	Metal cation
O	Oxide anion
NiO	Nickel oxide
LEDs	light-emitting diodes
TiO_2	Titanium oxide
UV	Ultraviolet
Ag_2O	Silver oxide
SnO_2	Tin oxide
MoO_3	Molybdenum oxide
V_2O_5	Vanadium oxide
WO_3	Tungsten oxide
Fe_2O_3	Iron oxide
Se	Selenium
Y^{+3}	Yttrium ions
XRD	X-ray diffraction
ZnO	Zinc oxide
Fe	Iron
$CuGaS_2$	Copper gallium sulfide
Bi_2S_3	Bismuth sulfide
θ	Bragg angle
λ	Wavelength
Δ	Path difference
d	Inter-planer spacing
n	Positive integer
p	Number of lattice planes
D	Crystallite size
β	The full width at half maximum (FWHM)
ε	Lattice strain
δ	Dislocation density
$SF\%$	Stacking faults
T	Transmittance
R	Reflectance
α	The absorption coefficient
A	Absorbance
t	Film thickness
E	Photon's energy
E_g	Optical energy band gap
B	Constant
E_u	Urbach energy
$\vec{E}$	Electric field
$\vec{H}$	Magnetic field

$\vec{j}$	Current density
$\vec{D}$	Electric field in the medium
$\vec{B}$	Magnetic field in the medium
ε	Complex dielectric function
μ	Complex magnetic permeability
σ	Complex electrical conductivity
w	Frequency of the light
$\vec{K}$	Complex propagation constant
ε_r	Real part of the dielectric constant
ε_{im}	Imaginary part of the dielectric constant
$\widetilde{N}_{complex}$	Complex refractive index
$\tilde{n}$	Real part of the complex refractive index
$\tilde{k}$	Imaginary part of the complex refractive index
EDX	The energy dispersive X-ray spectroscopy technique
SEM	Scanning electron microscope
Cu^{+2}	Copper ions
Sm^{+3}	Samarium ions
Fe^{+2} / Fe^{+3}	Iron ions

Chapter One

Introduction

In recent decades, metal oxide materials have gained interest due to their importance for scientific and technological applications. Metal oxides (MOs) are compounds that contain a metal cation (M) and an oxide anion (O). The metal oxide compounds are considered to be stable for the long term due to the high electronegativity of oxygen [1]. These materials possess modest to wide band gaps, which allow them to be classified as semiconductors or insulators [1]. Their distinctive properties make them possible for use in optoelectronics [2], photovoltaics [3], solar cells [4], and sensing applications [5]. On the other hand, it was reported that these materials are used as photocatalysts due to their ability to produce charge carriers when stimulated with an appropriate amount of optical energy [6]. In addition, metal oxide materials are used as hole/electron transport layers for light-emitting diodes [7]. Also as electrodes for supercapacitors [8] and storage devices [9]. Furthermore, heterojunctions that employ metal oxide as interfacing layers are beneficial for multifunctional electronic devices [10].

There are common metal oxide materials that are used for technological applications. For example, nickel oxide (NiO). This compound plays an important role in the fabrication of optoelectronic devices. It is used as a photocathode, electron blocking layer or hole transport layer for LEDs [11]. Another example is titanium oxide. TiO_2 nanobelts have great potential in the photocatalysis field. Many experiments showed that this oxide has excellent UV light photocatalytic activity [12]. Recent studies confirm that thin films of silver oxide (Ag_2O) prepared by the magnetron sputtering technique are considered a promising electrode material for supercapacitor applications [13]. In addition, it was reported that tin oxide (SnO_2) material can be used as an

electrode for energy harvesting and energy storage devices [14]. Another study revealed that some transition metal oxides, such as molybdenum oxide (MoO_3), vanadium oxide (V_2O_5) and tungsten oxide (WO_3) are used as front p-type contacts in silicon heterojunction solar cells [4]. Iron oxide (Fe_2O_3) is another oxide material that gains interest due to it is excellent electrical and magnetic properties. It is used for recording media, magnetic storage and solar energy applications [15]. Also, bismuth oxide (Bi_2O_3) compound is considered a promising material for different technological applications, such as optoelectronics [16].

Bismuth oxide (Bi_2O_3) films have five crystallographic polymorphs, $\alpha, \beta, \gamma, \delta$ and ω phases [17]. Therefore, these films are capturing the focus of the researchers owing to their wide range of applications. It was reported that Bi_2O_3 is considered a promising electrode material for supercapacitor applications [18]. As an example, the Bi_2O_3 is used as a negative electrode for a high-energy density asymmetric supercapacitor [18]. In addition, the amorphous bismuth oxide films were reported to have potential applications in memory devices [19], since they have highly uniform resistive switching properties. Even further, it was reported that the Bi_2O_3 films can be used as electronic switches and microwave resonators [20], as photoanodes [21] and as degrading material for methyl orange [22]. Bismuth oxide films are attractive for optoelectronic applications since they have moderate energy band gaps and a high dielectric constant [23].

Recent developing optoelectronic technology needs always calling for new devices with smart applications. Among the published reports, the doping effect is the most popular method used to enhance the optoelectronic performance of the material since it plays an important role in engineering the energy band gap. Literature data confirmed that the band gap and recombination rate of charge carriers for Bi_2O_3 are lowered when

doped by Se. Furthermore, the charge carrier and photocurrent densities are increased by doping [24]. Moreover, the conductivity and carrier mobility of Bi_2O_3 samples are improved when doping the pure samples with zinc [25]. Another report revealed the effect of Y^{+3} doping on Bi_2O_3 samples, the XRD results indicated that the Bi_2O_3 phase became more stable and the visible light absorption ability was enhanced compared to the pure sample [26].

Here in this work, we are motivated to explore the iron doping effects on Bi_2O_3 films, since this study is almost absent and there are many interesting features that have been achieved when using iron as a dopant in different materials. For example, it is reported that iron doping to ZnO remarkably decreased the energy band gap of ZnO, making it more appropriate for optoelectronic applications [27]. In addition, Fe doping on $CuGaS_2$ increased the light sensitivity of the materials by orders of magnitude and made it attractive for intermediate band solar cells [28]. The photosensitivity of Bi_2S_3 is also enhanced via iron doping [29]. Therefore, it was reported that the Fe doped Bi_2S_3 samples prepared by nebulized spray pyrolysis technique can be used for photodetector applications [29]. Importantly, the photocatalytic activity of Bi_2O_3 films prepared by sol gel method was improved by adding Fe^{+3} ions into Bi_2O_3 films [30].

This work will include different doping levels of iron in the Bi_2O_3 material. While the thermal evaporation technique was used to grow these films, X-ray diffraction, optical spectroscopy and scanning electron microscopy techniques were used to explore the properties of the prepared films and their possible applications. In chapter two of this thesis, some of the theoretical considerations that were needed to explain the experimental results will be reported. In the third chapter, we will display the experimental techniques that were employed to prepare and analyze the prepared films.

Chapter four shows the achieved results, interpretations, explanations, and discussions of the observations. Finally, chapter five displays the main conclusions of this research work.

Chapter Two

Theoretical Background

2.1 Semiconductor doping

Semiconductors are materials with electrical conductivity between conductors and insulators. Doping is a fundamental process in semiconductor fabrication. In this process, impurity atoms in specific amounts are added to a pure semiconductor in order to alter its properties [31]. A pure semiconductor is called an intrinsic material, while doped semiconductors are called extrinsic materials. The purpose of the doping process is to change the carrier concentration and create discrete defect states within the band gap in order to enhance the transfer of charges and alter the semiconductor properties.

2.1.1 Types of doping

There are two main types of doping in semiconductors: First, there is an N-type doping, in which elements of five valence electrons are added to the semiconductor crystal. These impurities create extra negative charge carriers in the material. Secondly, there is a P-type doping, in which elements of three valence electrons are added to the semiconductor crystal. These impurities create holes, resulting in positive charge carriers [31].

2.1.2 Semiconductor doping methods

There are several methods used in order to fabricate doped thin films. These methods are explained below.

The first method is simply called the doping method, in which the impurity atoms are introduced into the semiconductor material in order to modify its properties. There are several techniques that can be employed to dope thin films. This choice depends on the

material properties and their applications. These techniques are: ion implantation [32], chemical vapor deposition [33], physical vapor deposition [34], spin coating [35], molecular beam epitaxy [36], etc. In our work, we used thermal evaporation, which is a common physical vapor deposition technique, in order to dope bismuth oxide with iron.

The second method is the sandwiching method, also called the layer-by-layer method. In which we deposit a layer of intrinsic material that we want to dope on the surface of clean substrates using any deposition techniques, such as physical vapor deposition, chemical vapor deposition, ion coating, etc. After that, we deposit a layer of the dopant material on the surface of the intrinsic material in order to modify its properties using any one of the deposition techniques. We can control the layer thickness of the dopant material during the preparation process. Then we deposit another layer of the intrinsic material on the surface of the dopant layer [37]. At the end, the prepared thin film may undergo annealing or other processing in order to activate the dopants [37]. In this method, the choice of the intrinsic and doped materials, the order of layering, and the deposition techniques depend on the requirements of the applications of the doped thin film and its properties.

The third method is the laser doping method, which is commonly used in semiconductor device fabrication in order to modify the electrical properties of thin films. In this method, we deposit a layer of the pure semiconductor on the surface of a clean substrate. Then, we deposit a thin layer of the dopant material on the semiconductor surface using any deposition technique. After that, a laser beam with a specific energy and wavelength is used to melt the semiconductor surface [38]. The absorbed laser energy

activates the dopant material and allows the dopant to diffuse into the semiconductor material. Creating a doped semiconducting film. We can control the doping process by adjusting the laser parameters. After the doping process, the doped thin film may undergo many processing steps, such as annealing, in order to activate the dopants.

2.2 X-ray diffraction (XRD)

The X-ray diffraction technique is a powerful technique used to determine the crystal structure of a material in addition to the parameters related to the crystal structure [39]. Figure 2.1 below displays the basic components of an X-ray device [40]. This device consists of an X-ray tube (anode), a sample holder, and an X-ray detector.

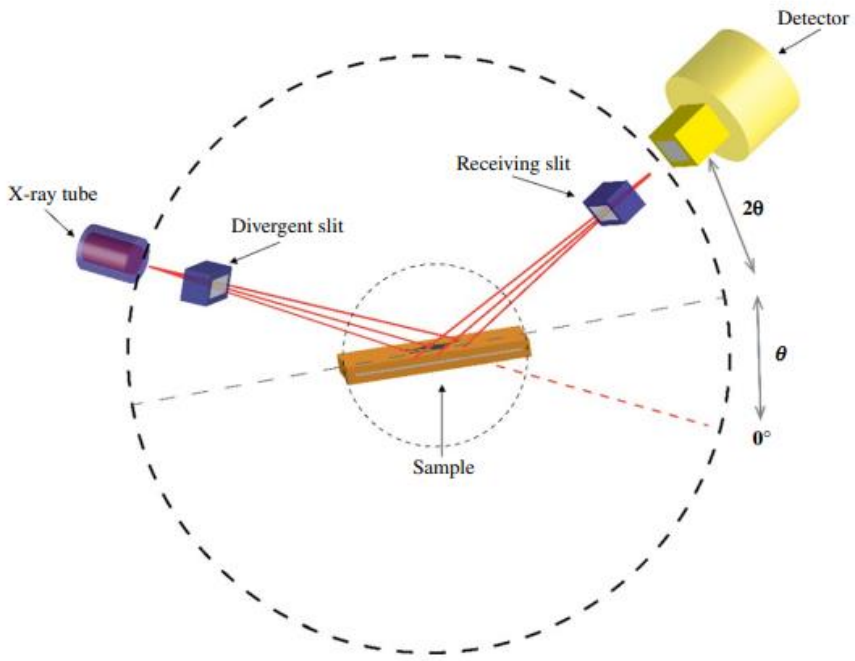

Figure 2.1. The schematic diagram of the X-ray diffractometer [40].

When X-rays are emitted from the anode and hit the sample, they are scattered in multiple directions by the atom's electrons. The scattered waves interfere with each other. The interference may be constructive or destructive. If the interfering waves are in phase, constructive interference occurs, and the crystalline nature appears.

Otherwise, if the interfering waves are out of phase, destructive interference occurs, and the amorphous nature appears [39]. It is clear from Figure 2.1 that the sample rotates at an angle θ, while the X-ray detector rotates at an angle 2θ. By scanning the sample at a range of 2θ angles, the X-ray detector records the X-ray signals and converts them to computer programs to analyze them. After the analysis process, the inter-planar spacing, the lattice constant, the lattice parameters, and the crystal structure are all determined.

2.2.1 Bragg's law

Bragg's law is the simplest way to understand the X-ray diffraction principle. Bragg's diffraction occurs when we subject a crystalline system to radiation of a wavelength value (λ) comparable to the distance between atomic planes, and this radiation is scattered by the atoms in a specular reflection form. Figure 2.2 below helps us derive Bragg's equation [41]. It's clear from Figure 2.2 that the wave 1 scattered by the lower plane traveled a longer distance than that traveled by wave 2. The difference in path is

$$\Delta = CB + BD \tag{2.1}$$

Constructive interference occurs when the path difference (Δ) between the two waves is equal to an integer multiple of the wavelength. Hence

$$\Delta = n\lambda \tag{2.2}$$

In addition, the path difference is equal to $2d \sin\theta$ according to Figure 2.2. So we get Bragg's law in the form

$$2d \sin\theta = n\lambda \tag{2.3}$$

Where d is the inter-planer spacing between two parallel lattice planes, θ is the angle between the incident (or reflected) beam and the surface of the atomic plane, which is

called the Bragg angle. n is the positive integer that represents the diffraction order, and λ is the wavelength of the X-ray beam. For a copper anode, the wavelength is equal to 1.5405 Å.

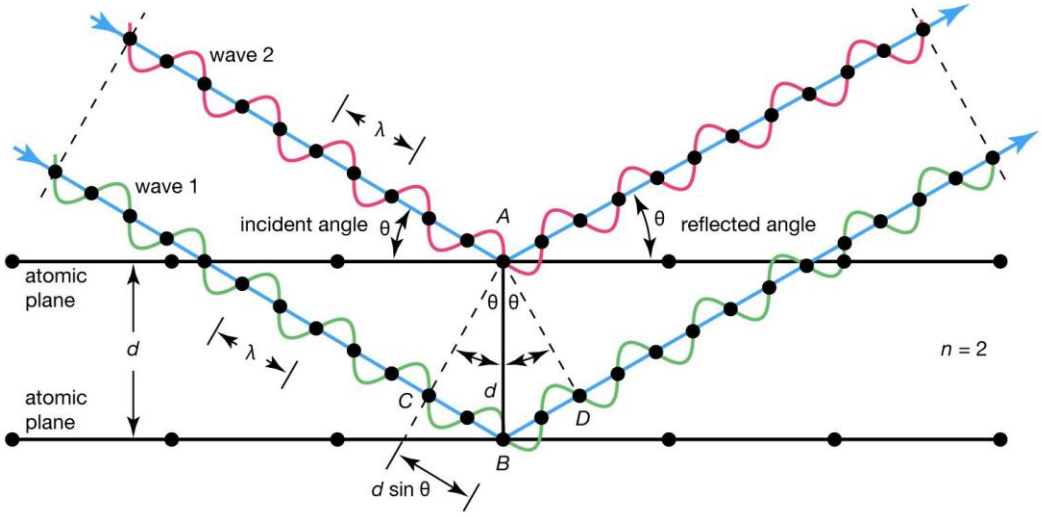

Figure 2.2. The schematic diagram of Bragg diffraction.

2.2.2 Scherrer equation

The Scherrer equation is a fundamental tool used to calculate the crystallite size of polycrystalline material [42]. This equation can be derived from Bragg's equation as follows [43]:

Consider a crystal composed of p lattice planes separated by a distance d. The crystallite size (D), which measures the mean size of nano-crystallite is equal to pd. When the incident angle changes from θ to $\theta + \delta$, the optical path difference can be written as [43]

$$2d\sin(\theta + \delta) = n\lambda + \Delta l \tag{2.4}$$

When the path difference is equal to the odd integer multiplied by $\frac{\lambda}{2}$ ($\Delta l = \frac{\lambda}{2}$), destructive interference occurs. For a crystal composed of p lattice planes, destructive interference occurs between the initial layer ($p = 0$) and the layer of $\frac{p}{2}$, the first layer ($p = 1$) and the layer of $\frac{p}{2} + 1$, the layer of $\frac{p}{2} - 1$ and p when the incident angle changes by a certain angle of δ. These relations are expressed as

$$\left(\frac{p}{2}\right) 2d \sin\theta = \left(\frac{p}{2}\right) n\lambda \tag{2.5}$$

$$\left(\frac{p}{2}\right) 2d \sin(\theta + \delta) = \left(\frac{p}{2}\right) n\lambda + \frac{\lambda}{2} \tag{2.6}$$

But we know from trigonometric identities that

$$\sin(\theta + \delta) = \sin\theta \cos\delta + \cos\theta \sin\delta \tag{2.7}$$

When δ is small, $\sin\delta \approx \delta$, $\cos\delta \approx 1$

The trigonometric identity becomes

$$\sin(\theta + \delta) = \sin\theta + \delta \cos\theta \tag{2.8}$$

Substitute equation (2.8) into equation (2.6) to get

$$\left(\frac{p}{2}\right) 2d(\sin\theta + \delta \cos\theta) = \left(\frac{p}{2}\right) n\lambda + \frac{\lambda}{2} \tag{2.9}$$

$$\left(\frac{p}{2}\right) 2d \sin\theta + \left(\frac{pd}{2}\right) 2\delta \cos\theta = \left(\frac{p}{2}\right) n\lambda + \frac{\lambda}{2} \tag{2.10}$$

Compared with equation (2.5), and because $D = pd$

$$D\delta \cos\theta = \frac{\lambda}{2} \tag{2.11}$$

Since the angle $\theta - \delta$ is the angle at which the diffraction peak appears, and the angle $\theta + \delta$ is the angle at which the diffraction peak vanishes, δ is the half width at half maximum, so

$$\beta \approx 2\delta \tag{2.12}$$

Where β is the full width at half maximum (FWHM).

$$\beta = \frac{\lambda}{D\ cos\theta} \tag{2.13}$$

The accurate Scherrer equation can be obtained from

$$\beta = \frac{0.94\ \lambda}{D\ cos\theta} \tag{2.14}$$

Where β is the full width at half maximum, λ is the wavelength of an X-ray, D is the crystallite size of nano-crystalline material, and θ is the diffraction angle. Figure 2.3 below illustrates the full width at half maximum intensity [43]. The value of 0.94 is a percolation number computed by theoretical considerations that are out of this thesis scope.

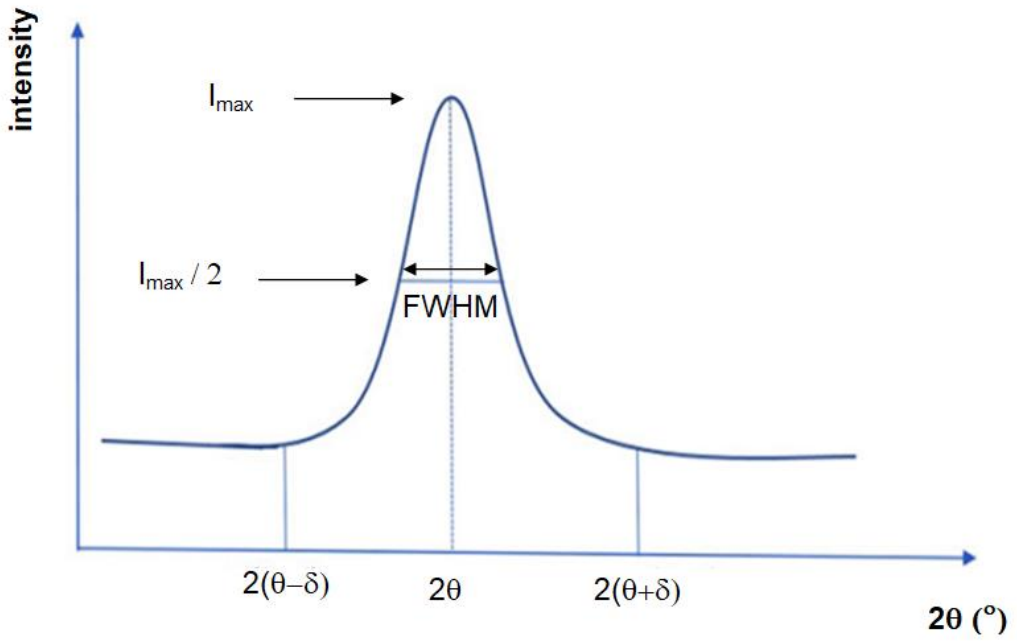

Figure 2.3. The full width at half maximum (FWHM) [43].

2.2.3 Structural parameters

As well as using the XRD patterns to determine the crystal structure, they are also used to calculate a lot of structural parameters. The most important parameters are crystallite size (D), lattice strain (ε), dislocation density (δ), and stacking faults ($SF\%$). These

parameters are calculated from the broadening width (β) of the most intensive peak. The crystallite size (D) is the mean size of nano-crystallites in nano-crystalline materials [44]. It is calculated from the Scherrer equation as follows [43]:

$$D = \frac{0.94\,\lambda}{\beta\,cos\theta} \tag{2.15}$$

The lattice strain (ε) is expressed the distortion of the lattice constant relative to the original one [45]. It is calculated from this equation [46]:

$$\varepsilon = \frac{\beta}{4\,tan\,\theta} \tag{2.16}$$

The strain has two types: uniform and non-uniform. The uniform strain causes changes in the lattice parameters. This appears in the deflection of the observed peak without causing a peak to broaden. However, the non-uniform strain causes a shift of atoms from their locations regularly. Therefore, the peak broadening appears. Figure 2.4 below shows the strain types [47].

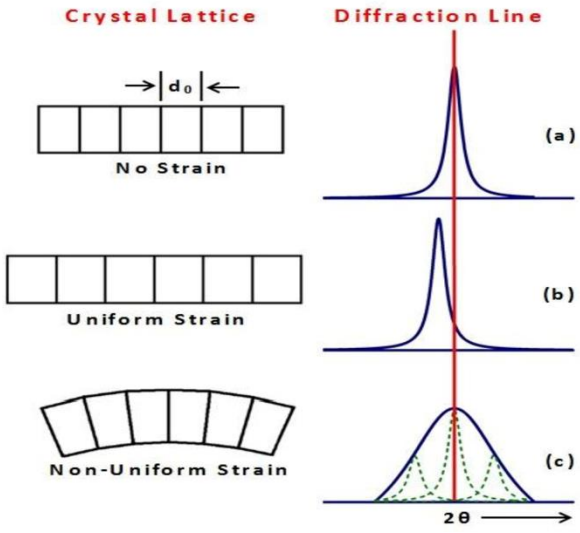

Figure 2.4. The effect of strain types on the atoms and the observed peak [47].

The dislocation density (δ) is measured by dividing the length of dislocation lines to the volume of the unit cell [45]. It can be calculated using the following equation [46]:

$$\delta = \frac{15\,\varepsilon}{a\,D}\ lines/cm^2 \tag{2.17}$$

Where ε is the lattice strain, D is the crystallite size and a is the lattice constant along the a-axis.

The stacking faults ($SF\%$) is a planer defect in which the proper order of planes is interrupted. It is calculated using the following formula [46]:

$$SF\% = \frac{2\pi^2\beta}{45\sqrt{3\ tan\theta}} \times 100\% \tag{2.18}$$

2.2.4 Classification of solids and crystal structures

Solid elements and their compounds are classified according to their crystal structures into amorphous, single crystalline, and polycrystalline materials [48]. In amorphous materials, the atoms and molecules are not arranged in any specific order. In contrast, in the crystalline material, the atoms or molecules are arranged in regular and repeated patterns. However, a polycrystalline material is composed of many small grains separated by grain boundaries. The arrangement of atoms is nearly identical within each grain, but the orientation of the atoms is different. Figure 2.5 illustrates the arrangement of atoms in amorphous, polycrystalline, and single crystalline materials, respectively [31].

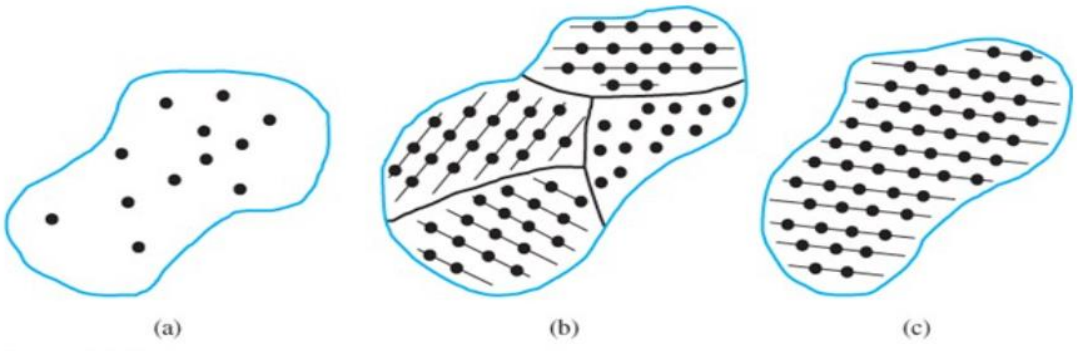

Figure 2.5. Schematics of three general types of crystals: (a) amorphous, (b) polycrystalline and (c) single crystalline material [31].

Crystal consists of a repeated pattern of unit cells arranged into a lattice. In three dimensions, the size and shape of the unit cell can be characterized by the length of three axes (a_1, a_2, a_3) and the angle between them (α, β, γ) [48]. Atoms can be arranged in crystals in fourteen different three-dimensional configurations known as Bravais lattices. These Bravais lattices are classified into seven families according to the length of the axes, angle between the axes, and symmetry properties. Table 2.1 below displays the seven families and their conditions [49].

Table 2.1. The seven families of crystal lattices and their conditions [49].

Crystal lattice	Number of Bravais lattice	Conditions
Cubic	3	$a_1=a_2=a_3$ $\alpha=\beta=\gamma=90^0$
Hexagonal	1	$a_1=a_2\neq a_3$ $\alpha=\beta=90^0, \gamma=120^o$
Trigonal	1	$a_1=a_2=a_3$ $\alpha=\beta=\gamma<120^o\neq90^0$
Tetragonal	2	$a_1=a_2\neq a_3$ $\alpha=\beta=\gamma=90^0$
Orthorhombic	4	$a_1\neq a_2\neq a_3$ $\alpha=\beta=\gamma=90^0$
Monoclinic	2	$a_1\neq a_2\neq a_3$ $\alpha=\beta=90^0\neq\gamma$
Triclinic	1	$a_1\neq a_2\neq a_3$ $\alpha\neq\beta\neq\gamma\neq90^0$

2.3 Optical properties

The optical property term describes how a material behaves when electromagnetic radiation (light) is incident on its surface. The incident electromagnetic radiation may be transmitted via the material, reflected outside the material, or propogated through the material. When light propagates through the optical medium, there are four phenomena that can occur. These phenomena are: refraction, absorption, luminescence,

and scattering [50]. Figure 2.6 displays the interaction of electromagnetic radiation with the optical medium.

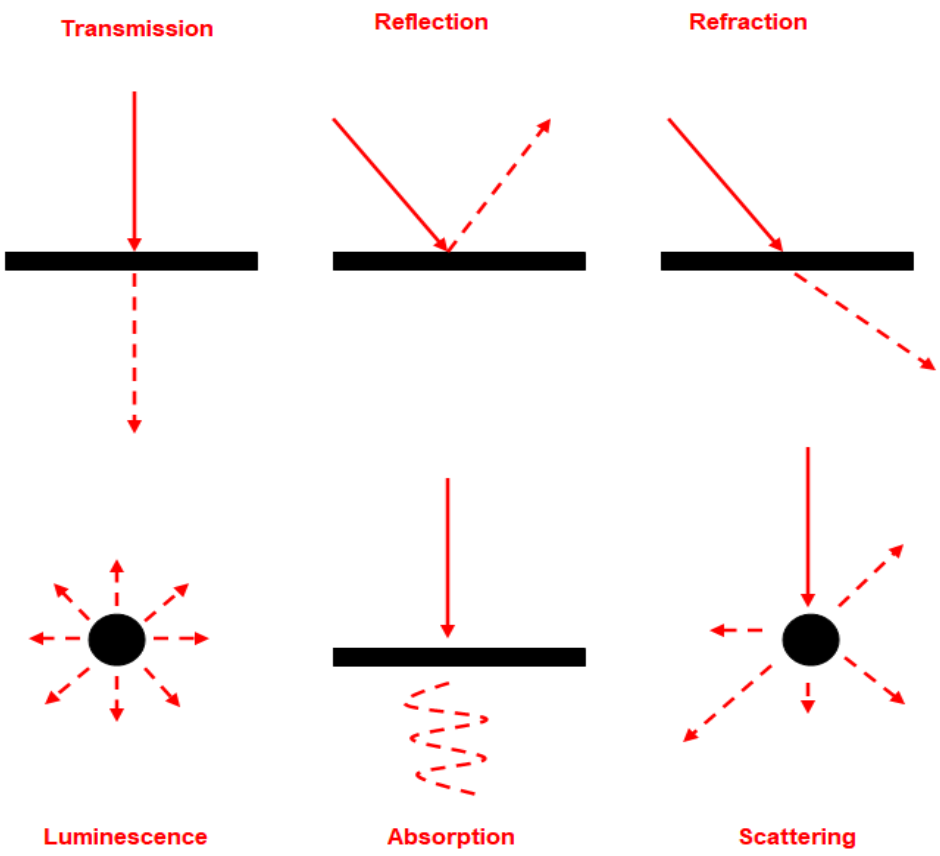

Figure 2.6. The interaction of light with matter.

Transmittance is defined as the ratio of the intensity transmitted by a medium to the intensity entering the medium.

Reflectance is defined as the phenomenon in which light encounters a surface or boundary between two materials and returns to the same material.

Refraction is defined as the bending of light at the interface due to the reduction of the light velocity when it propagates through the medium [50]. The refraction of light phenomenon is described by Snell's law as

$$n_1 \sin\theta_1 = n_2 \sin\theta_2 \tag{2.19}$$

Absorption occurs when the frequency of incident light is resonant with the frequency of solid material oscillations, then the light will be absorbed [50].

Luminescence is defined as the spontaneous emission of light due to the excitation of atoms and the transfer of electrons from the higher-energy state to the lower-energy state [50].

Scattering occurs when the light deviates from it is original path due to interacting with the medium [50].

The analysis of optical properties includes measurements of the transmittance (T) and reflectance (R) spectra in order to calculate the absorption coefficient (α) spectra, which is considered one of the most important tools to understand the band structure, the band gap energy, and the dielectric constant for prepared materials.

2.3.1 The absorption coefficient (α)

The absorption coefficient (α) determines how far light of a specific wavelength can penetrate inside a material before being absorbed. If a material has a high absorption coefficient, light can be readily absorbed and excited electrons from the valence band to the conduction band. In contrast, if a material has a low absorption coefficient, light will be poorly absorbed. The absorption coefficient (α) depends on the material in addition to the wavelength of light being absorbed.

When a monochromatic light beam with intensity I_0 propagates in the z direction and passes through a medium with thickness dz, it is intensity will decrease and be equal to I. At any point, the decrease in light intensity with the thickness of the absorbing medium is directly proportional to the intensity of the light. This law is known as Beer-Lambert law, which can be expressed mathematically as [50]:

$$-\frac{dI}{dz} \propto I \tag{2.20}$$

Or it can be written in a form

$$-\frac{dI}{dz} = \alpha I \tag{2.21}$$

Since $-\frac{dI}{dz}$ is the rate at which the intensity decreases with thickness and α is the absorption coefficient, by rearrangement of equation (2.21) and integration, we get

$$I(z) = I_o\, e^{-\alpha z} \tag{2.22}$$

Where $I(z)$ is the intensity after traveling a distance z in the medium, I_o is the light intensity at $z = 0$, α is the absorption coefficient, and z is the material thickness.

In order to derive a formula for the absorption coefficient based on the Beer-Lambert law, we want to define the absorbance (A) of the material in terms of its transmissivity (T) and reflectivity (R). Transmissivity (T) describes the ability of a material to transmit electromagnetic radiation. The transmissivity of an optical medium of thickness l is given by [50]:

$$T = (1 - R_1)(1 - R_2)\, e^{-\alpha l} \tag{2.23}$$

Since R_1 and R_2 are defined as the reflectivities of the front and back surfaces, respectively. Therefore, the terms $(1 - R_1)$ and $(1 - R_2)$ describe the transmission of

the front and back surfaces, respectively. The term $e^{-\alpha l}$ represents the exponential decay in intensity due to the absorption, as the Beer-Lambert law suggested. If the reflectivities of front and back surfaces are equal to R, as they usually are, the equation (2.23) is simplified to

$$T = (1 - \mathrm{R})^2 \, e^{-\alpha l} \tag{2.24}$$

The absorbance (A) of a prepared film is the quantity of light that is absorbed by the medium. It is defined as the logarithm of the ratio of incident power to transmitted power through the medium, which can be mathematically expressed as:

$$A = \ln\left(\frac{P_o}{P}\right) = \ln\left(\frac{I_o}{I}\right) = -\ln\left(\frac{I}{I_o}\right) \tag{2.25}$$

By comparing equations (2.22) and (2.23) we get

$$\frac{I}{I_o} = \frac{T}{(1 - R_1)(1 - R_2)} \tag{2.26}$$

By substituting of equation (2.26) into (2.25), we get

$$A = -\ln\left(\frac{T}{(1 - R_1)(1 - R_2)}\right) \tag{2.27}$$

The absorption coefficient (α) is connected to the absorbance (A) of the prepared film using the following relation:

$$A = \alpha \, t \tag{2.28}$$

Hence, the absorption coefficient for deposited film is

$$\alpha = -\frac{1}{t}\ln\left(\frac{T}{(1 - R_1)(1 - R_2)}\right) \tag{2.29}$$

In our work, R_1 and R_2 represent the reflectivity of glass and deposited films, respectively, and t is the layer thickness of the prepared thin film.

2.3.2 Direct and indirect transitions

The band gap energy is the energy needed to transfer an electron from the valence band to the conduction band [51]. The band gap of a semiconductor can be classified into two types: a direct band gap or an indirect band gap, as shown in Figure 2.7. In the direct band gap, the maximum energy level of the valence band and the minimum energy level of the conduction band are located at the same momentum value. In this case, any photon of energy equal to the energy gap can produce an electron-hole pair easily since it doesn't need to be given very much momentum. In contrast, the indirect band gap can be characterized as a phenomenon in which the maximum energy level of the valence band is misaligned with the minimum energy level of the conduction band with respect to momentum. In order to produce an electron-hole pair in an indirect band gap semiconductor, an electron must undergo a significant change in its momentum for a photon of energy equal to the energy gap. This process required the interaction of an electron with a photon to gain energy, as well as with the lattice vibration called a phonon to change momentum.

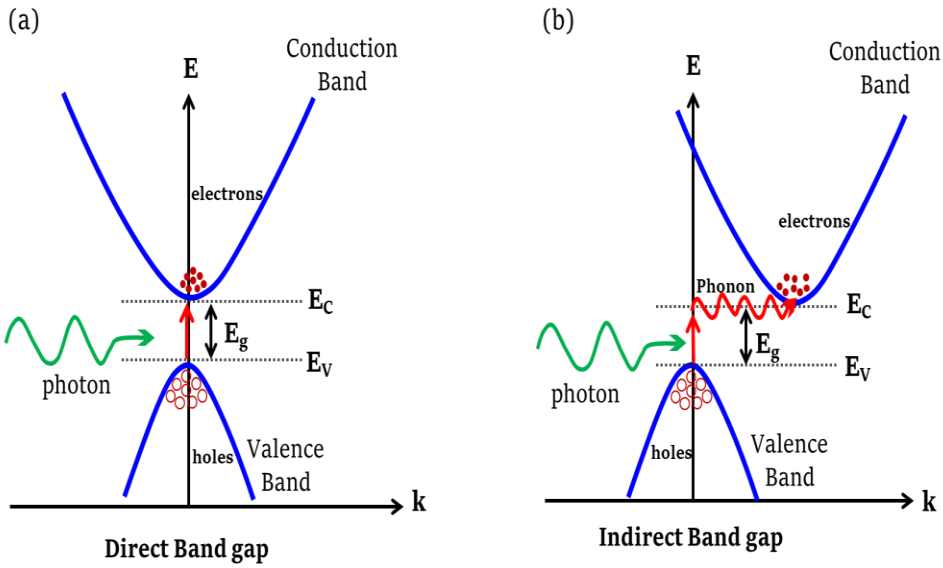

Figure 2.7. The schematic diagram of (a) direct and (b) indirect band gaps [52].

2.3.3 Tauc's equation

Tauc's equation is a fundamental method used to estimate the optical energy band gap of semiconductors using the absorption coefficient spectra. Tauc's equation supposes that the energy-dependent absorption coefficient (α) can be described by the following relation [51].

$$(\alpha E)^{1/p} = B\left(E - E_g\right) \tag{2.30}$$

Where α is the absorption coefficient, E is the photon's energy, E_g is the optical energy band gap, B is a constant and p is a factor that describes the nature of the electron transition. The factor p is theoretically equal to $\frac{1}{2}$, 2 , $\frac{3}{2}$, 3 corresponding to the direct allowed, indirect allowed, direct forbidden, and indirect forbidden transitions between the valence and conduction bands, respectively.

In order to calculate the band gap energy, we plot $(\alpha E)^{1/p}$ versus E and take the widest range of linear data in the high absorption region upon linear fitting. The band gap energy is determined by the intercept of the E-axis.

2.3.4 Band tails

The Urbach tail is the exponential dependence of the absorption coefficient spectra on the photon energy [53]. This behavior is a well-known phenomenon in the optical properties of insulators, amorphous, and crystalline semiconductors. These tails arise near the optical band edge due to the presence of disorders, impurities, and the electron-phonon interaction in the absorption processes [54].

Urbach's rule is described as follows:

$$\alpha = \alpha_o \, e^{E/E_u} \tag{2.31}$$

Where α is the absorption coefficient, α_o is a constant, E is the photon energy, and E_u is the Urbach energy. By taking the logarithm of the two sides of the equation (2.31), we get a straight line equation

$$\ln \alpha = \ln \alpha_o + \left(\frac{E}{E_u}\right) \tag{2.32}$$

The Urbach energy is the inverse of the slope of the straight line in $\ln \alpha - E$ plot.

2.3.5 The refractive index and the dielectric constant spectra

The complex optical conductivity and the complex dielectric constant are introduced through Maxwell's equations as follows (assuming there is no charge density in the absence of incident light) [55].

$$\vec{\nabla} \times \vec{E} = -\frac{\partial \vec{B}}{\partial t} \tag{2.33}$$

$$\vec{\nabla} \times \vec{H} = \vec{j} + \frac{\partial \vec{D}}{\partial t} \tag{2.34}$$

$$\vec{\nabla}.\vec{D} = 0 \tag{2.35}$$

$$\vec{\nabla}.\vec{B} = 0 \tag{2.36}$$

Since $\vec{E}$, $\vec{H}$, and $\vec{j}$ are the electric field, magnetic field, and current density, respectively. While $\vec{D}$ and $\vec{B}$ are the electric and magnetic fields in the medium. In linear optics, the equations relating $\vec{D}$, $\vec{B}$ and $\vec{j}$ to $\vec{H}$ and $\vec{E}$ fields can be written in the form

$$\vec{D} = \varepsilon \vec{E} \tag{2.37}$$

$$\vec{B} = \mu \vec{H} \tag{2.38}$$

$$\vec{j} = \sigma \vec{E} \tag{2.39}$$

Equations (2.37), (2.38) and (2.39) respectively, are defined the concepts of the complex dielectric function (ε), the complex magnetic permeability (μ), and the complex electrical conductivity (σ).

By taking the curl of equation (2.33) and eliminating $\overrightarrow{B}$ and $\vec{\nabla} \times \vec{H}$ from equations (2.38) and (2.34), respectively, we get

$$\vec{\nabla} \times \left(\vec{\nabla} \times \vec{E}\right) = -\mu\left(\frac{\partial \vec{j}}{\partial t} + \frac{\partial^2 \vec{D}}{\partial t^2}\right) \tag{2.40}$$

Substituting equations (2.39) and (2.37) into equation (2.40) to get

$$\vec{\nabla} \times \left(\vec{\nabla} \times \vec{E}\right) = -\left(\mu\sigma \frac{\partial \vec{E}}{\partial t} + \mu\varepsilon \frac{\partial^2 \vec{E}}{\partial t^2}\right) \tag{2.41}$$

The left hand side of equation (2.41) can be simplified with the help of vector identity

$$\vec{\nabla} \times \left(\vec{\nabla} \times \vec{E}\right) = \vec{\nabla}\left(\vec{\nabla}.\vec{E}\right) - \vec{\nabla}^2 \vec{E} \tag{2.42}$$

If there is no charge density, $\vec{\nabla}.\vec{E}$ is equal to zero and the equation (2.42) becomes

$$\vec{\nabla}^2\vec{E} = \mu\sigma\frac{\partial\vec{E}}{\partial t} + \mu\varepsilon\frac{\partial^2\vec{E}}{\partial t^2} \tag{2.43}$$

By taking the curl of equation (2.34) and eliminating $\vec{\nabla}\times\vec{j}$ and $\vec{\nabla}\times\vec{D}$ from equations (2.39) and (2.37), respectively, we get

$$\vec{\nabla}^2\vec{H} = \mu\sigma\frac{\partial\vec{H}}{\partial t} + \mu\varepsilon\frac{\partial^2\vec{H}}{\partial t^2} \tag{2.44}$$

The solutions of equations (2.43) and (2.44) are sinusoidal solutions in the form

$$\vec{E} = E_0 e^{i(\vec{K}.\vec{r}-wt)} \tag{2.45}$$

$$\vec{H} = H_0 e^{i(\vec{K}.\vec{r}-wt)} \tag{2.46}$$

Where w is the frequency of the light and $\vec{K}$ is the complex propagation constant. The real part of the complex propagation constant can be defined as a wave vector, while the imaginary part represents the attenuation of the wave inside the material and corresponds to energy dissipation.

Substituting the sinusoidal solution (2.45) into equation (2.43) to get

$$K^2 = \mu\varepsilon w^2 + i\mu w\sigma \tag{2.47}$$

If there are no losses in the energy, K would be a real number and identified as a wave vector as

$$K_0 = w\sqrt{\mu\varepsilon} \tag{2.48}$$

If there are losses in energy in the conducting medium, K would be a complex number defined as

$$K = w\sqrt{\mu\varepsilon_{complex}} \tag{2.49}$$

Since the complex dielectric function is defined as

$$\varepsilon_{complex} = \varepsilon + \frac{i\sigma}{w} = \varepsilon_r + i\varepsilon_{im} \tag{2.50}$$

Since ε_r and ε_{im} are the real and imaginary parts of the dielectric constant.

$$\varepsilon_{complex} = \frac{i}{w}\left[\sigma + \frac{\varepsilon w}{i}\right] = \frac{i}{w}\sigma_{complex} \tag{2.51}$$

Where we defined complex conductivity as

$$\sigma_{complex} = \sigma - i\varepsilon w \tag{2.52}$$

The complex dielectric function and the complex conductivity are related to the observables that are measured in the laboratory, such as absorption, and to the properties of the solid material, such as effective mass and carrier density. In order to find these relations, consider a wave propagating in the z-direction. By substituting K into equation (2.45), we get a plane wave in a form

$$\vec{E}(z,t) = E_o e^{-iwt} e^{\left(iwz\sqrt{\varepsilon\mu}\sqrt{1+\frac{i\sigma}{\varepsilon w}}\right)} \tag{2.53}$$

In free space, $\varepsilon = \varepsilon_0$, $\mu = \mu_0$, $\sigma = 0$. The equation (2.53) is reduced to a simple plane wave solution.

$$\vec{E} = E_0 e^{i(Kz-wt)} \tag{2.54}$$

Where $K = K_0 = w\sqrt{\varepsilon_0\mu_0}$ and $c = \frac{1}{\sqrt{\mu_0\varepsilon_0}}$, since c is the speed of electromagnetic wave in free space.

If the electromagnetic wave is propagating in a medium of finite electrical conductivity, the equation (2.53) can be written in the form.

$$\vec{E}(z,t) = E_o e^{\frac{-w\tilde{k}z}{c}} e^{i(\frac{w\tilde{n}z}{c} - wt)} \tag{2.55}$$

Since $\tilde{n}$ and $\tilde{k}$ are the real and imaginary parts of the complex refractive index, respectively, which can be defined as

$$\tilde{N}_{complex} = c\sqrt{\mu\varepsilon_{complex}} = c\sqrt{\mu\varepsilon(1 + \frac{i\sigma}{w\varepsilon})} = \tilde{n}(w) + i\tilde{k}(w) \tag{2.56}$$

The real part of refractive index ($\tilde{n}$) is defined as the ratio of the speed of light in free space to the speed of light in the medium [56]. The imaginary part ($\tilde{k}$) is called the extinction coefficient since it measures the amount of light absorbed at a given wavelength [56]. Both the real and imaginary parts are frequency-dependent.

For non magnetic material, we can take $\mu = \mu_0$. The equation (2.56) can be written as

$$\varepsilon_{complex} = \varepsilon_0 \ (\tilde{N}_{complex})^2 = \varepsilon_0 \ (\tilde{n} + i\tilde{k})^2 \tag{2.57}$$

$$\varepsilon_{complex} = \varepsilon_0(\tilde{n}^2 - \tilde{k}^2) + i2\tilde{n}\tilde{k}\varepsilon_0 \tag{2.58}$$

Comparing equations (2.50) and (2.58) to get

$$\varepsilon_r = \varepsilon_0(\tilde{n}^2 - \tilde{k}^2) \tag{2.59}$$

$$\varepsilon_{im} = \varepsilon_0(2\tilde{n}\tilde{k}) \tag{2.60}$$

2.3.6 Drude-Lorentz model

Drude Lorentz model treats the valence electrons of the metals as free electrons. When an external electric field is applied, the free electrons accelerate according to the classical equations. The drift velocity of the free electrons is described according to the classical equation of motion as [55]

$$m\frac{dv}{dt} + \frac{mv}{\tau} = e\,E_0 e^{-iwt} \tag{2.61}$$

The first term is the acceleration of electrons, the second term describes the frictional damping or dissipative force of the medium and the sinusoidally time dependent electric field describes the driving force. Since the applied electric field is sinusoidal, the electrons will undergo a sinusoidal motion as follows

$$v = v_0 e^{-iwt} \tag{2.62}$$

Substituting equation (2.62) into equation (2.61) to get

$$\left(-imw + \frac{m}{\tau}\right) v_0 = e\,E_0 \tag{2.63}$$

Therefore, we can write

$$v_0 = \frac{e\,E_0}{\frac{m}{\tau} - imw} \tag{2.64}$$

Also we know that the current density is related to the carrier density and drift velocity as

$$\vec{j} = nev_0 = \sigma E_0 \tag{2.65}$$

Substituting equation (2.64) into equation (2.65) to get

$$\sigma = \frac{ne^2\tau}{m(1 - iw\tau)} \tag{2.66}$$

Consider that the only conduction mechanism that we are treating now is the free carrier mechanism. Therefore, we will consider all other contributions to σ in terms of ε_{core} (core dielectric constant) to obtain for the total complex dielectric function

$$\varepsilon_{complex} = \varepsilon_{core} + \frac{i\sigma}{w} \tag{2.67}$$

By substitution the equation (2.66) into equation (2.67) we get

$$\varepsilon_{complex} = \varepsilon_{core} + \frac{i}{w}\frac{ne^2\tau}{m(1 - iw\tau)} \cdot \frac{(1 + iw\tau)}{(1 + iw\tau)} = \varepsilon_r + i\varepsilon_{im} \tag{2.68}$$

Then the real and imaginary parts of the dielectric constant can be written as

$$\varepsilon_r = \varepsilon_{core} - \frac{ne^2\tau^2}{m(1+w^2\tau^2)} \tag{2.69}$$

$$\varepsilon_{im} = \frac{ne^2\tau}{wm(1+w^2\tau^2)} \tag{2.70}$$

Chapter Three

Experimental Details

In this chapter, we present all the experimental details used to fabricate pure and iron doped bismuth oxide films, in addition to the multiple techniques that were used to explore the structural, morphological, compositional, optical and dielectric properties of the fabricated films.

3.1 Thin film preparation

The thermal evaporation technique is one of the common methods used to deposit pure or doped materials on the surface of various substrates or multiple materials in a layered structure. Therefore, in this part, we will show all the steps that we applied in order to prepare pure and iron-doped bismuth oxide samples via the thermal evaporation technique. This part covers all the preparation steps from substrate cleaning until producing films in their final forms.

3.1.1 Substrate Cleaning

In order to prepare thin films, good-quality glass slides were chosen as substrates. Firstly, we selected a group of slides that had no scratches or cracks, then we sprayed them with alcohol and dried them with a hair dryer in order to determine the location of the dirt and stains accurately. After that, these slides were cleaned using a softening sponge, dishwashing liquid, and distilled water. During the cleaning process, we focused on stains and cleaned them well. These steps were repeated twice in order to obtain clean films. Then, the clean slides were placed inside a beaker filled with ethyl alcohol (97%) and covered by aluminum foil for a period of time in order to crack proteins stuck on them. As a final step, the clean slides were dried, and it was ensured

that no films contained scratches or cracks, and they were kept in a clean place until the substrate holder was prepared. The substrate holder was cleaned using alcohol and covered by aluminum foil. The cleaned glass slides are adhered to the substrate holder using thin adhesive on the edges. Figure 3.1 displays the clean slides and the substrate holder.

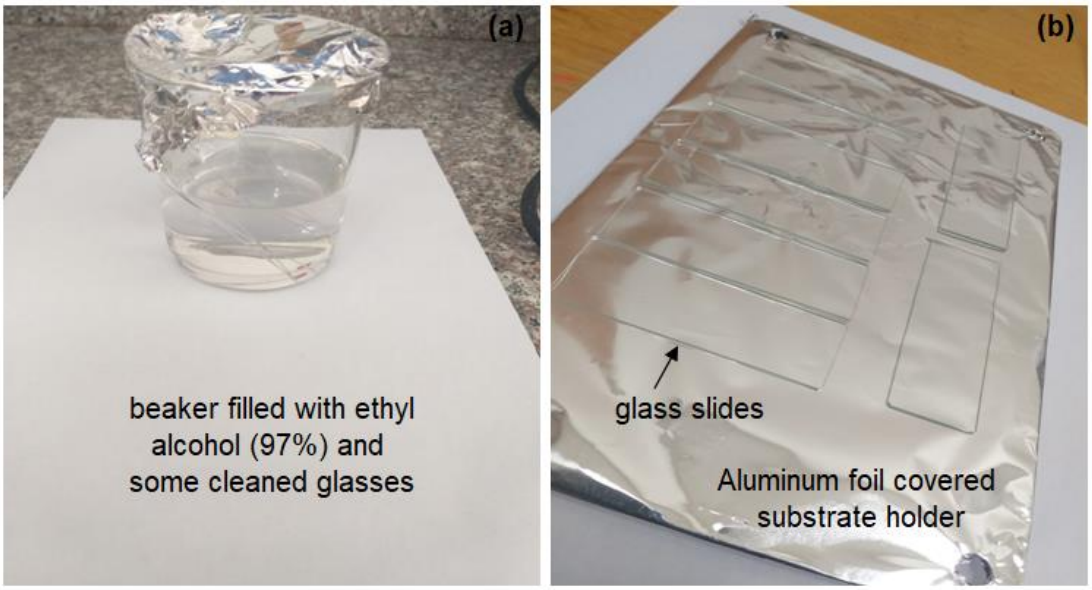

Figure 3.1. (a) Clean glass slides kept in alcohol media and (b) clean glass slides mounted onto a substrate holder.

3.1.2 Powder mixing

The first step that was applied in order to prepare iron-doped bismuth oxide thin films was mixing a specific amount of bismuth oxide powder with different amounts of iron powder. Three mixtures are produced by mixing 0.3 gm of bismuth oxide powder (99.999% trace metals basis Alfa Aesar) with 0.01 gm, 0.02 gm and 0.04 gm of iron powder (99.999% Alfa Aesar), respectively. The bismuth oxide powder, the iron powder and the electronic micro-balance used for mass measurements are shown in Figure 3.2. To produce a homogeneous mixture, the Fritsch Pulverisette 23 mini mill grinder shown in Figure 3.3 was used. This machine produces a homogeneous mixture since it grinds the sample through friction between the grinding bowl and grinding balls.

This device was operated for 10 minutes to perform 50 oscillations per second. The weight content of iron powder in bismuth oxide powders was 3.0%, 6.0% and 13.0%. Therefore, the mixture powder composed of 0.3 gm of Bi_2O_3 and 0.01 gm of Fe is abbreviated as $FBO-03$ sample. Those composed of 0.3 gm of Bi_2O_3 and 0.02 gm of Fe are abbreviated as $FBO-06$ samples. The third samples containing 0.04 gm of Fe are abbreviated as $FBO-13$ samples and the pure bismuth oxide samples are abbreviated as $FBO-00$ samples.

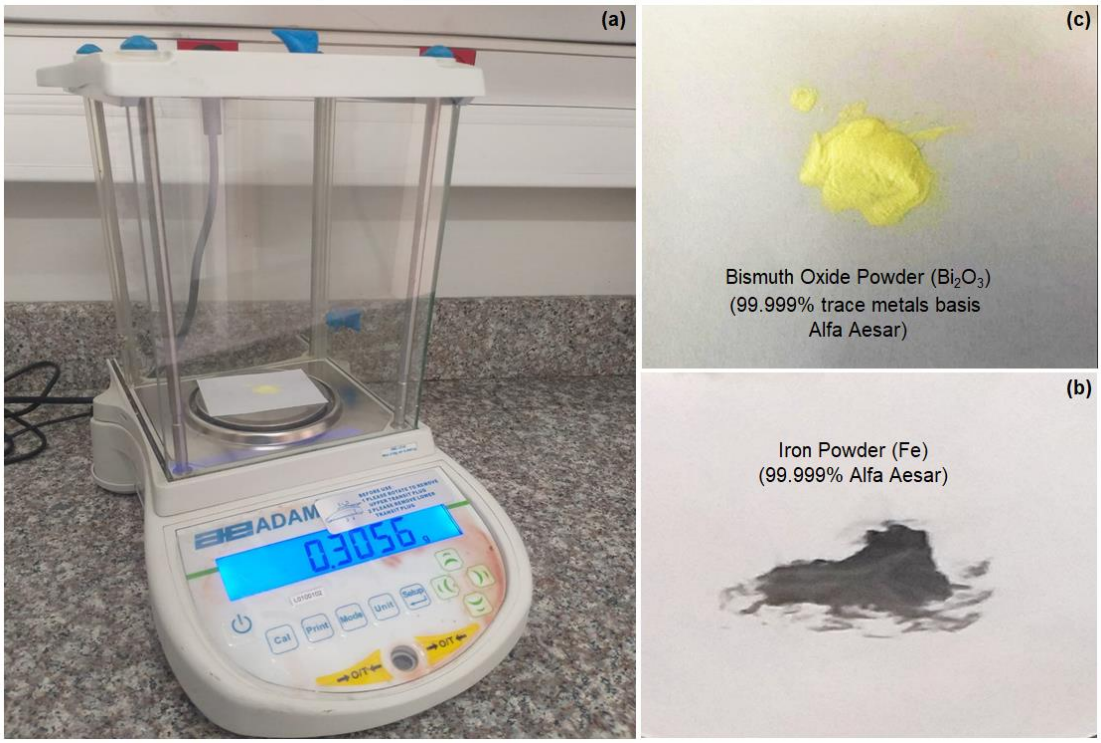

Figure 3.2. (a) Electronic micro balance, (b) iron powder and (c) bismuth oxide powder.

Figure 3.3. The Fritsch Pulverisette 23 mini mill grinder with grinding bowl and balls.

3.1.3 Deposition process and thin film preparation

In this process, the thermal evaporation technique was applied four times in order to prepare the pure and iron-doped bismuth oxide films. These films are prepared with the help of the VCM 600 thermal vacuum evaporator system under high vacuum pressure. The system is shown in Figure 3.4. During the preparation process of thin films, it is necessary to ensure that the bell jar and the evaporator system are cleaned. Also, since the tungsten material has low evaporation pressure, the tungsten boat specified for bismuth oxide is matched with the evaporation system and the substrate holder is fixed in a specific location.

In the 1st cycle, in order to prepare pure Bi_2O_3 films, we loaded 0.3 gm of bismuth oxide powder (99.999% trace metals basis Alfa Aesar) in the tungsten boat, then closed the bell jar and vent valve and turned on. When the vacuum pressure reached $\sim 10^{-4}$ mbar, we started the evaporation mechanism and opened the shutter after 2 minutes at

the current value of 50 A. The evaporation mechanism takes nearly 5 minutes. A layer of thickness 0.5 μm of pure Bi_2O_3 films was deposited onto clean glass substrates. The thickness of the films was monitored with the help of an INFICON STM-2 thickness monitor connected with the STM-Xwin23 software program, as shown in Figure 3.5. The produced films and the remaining powder that was melted in the boat were maintained inside the bell jar until the chamber was cooled. Then the produced films were kept in a clean place until studied, and the tungsten boat was burned in order to remove the molten material stuck in it and make it ready for use for the second time.

The same procedure was repeated in order to evaporate the homogeneous mixture powder of Fe and Bi_2O_3 on the clean glass substrates. In the second, third, and fourth times. The evaporation process started when the vacuum pressure reached $\sim 10^{-4}$ mbar. The same evaporation conditions were repeated to deposit a layer of thickness 0.5 μm of the $FBO-03$, $FBO-06$ and $FBO-13$ samples in the second, third and fourth times. The optical images of the real samples are shown in Figure 3.6. And the geometrical design of the prepared films is shown in Figure 3.7.

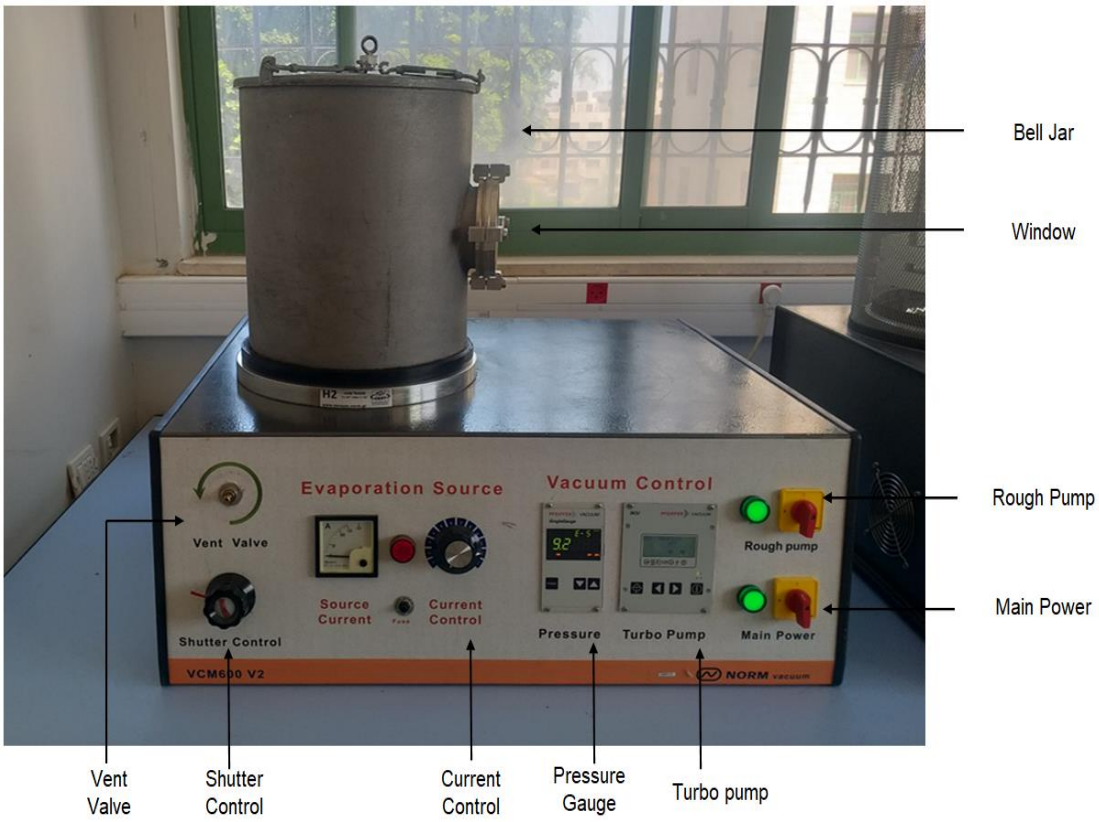

Figure 3.4. The VCM 600 thermal vacuum evaporator system used to prepare pure and Fe-doped Bi_2O_3 thin films.

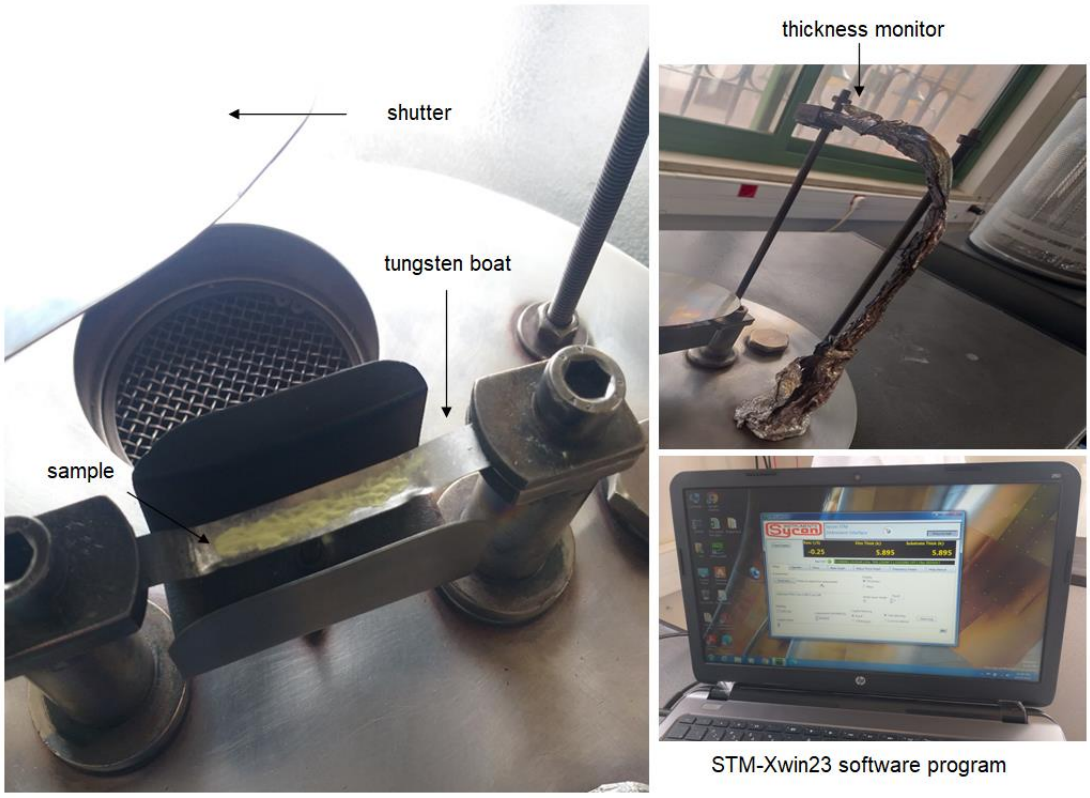

Figure 3.5. The components of the evaporator system inside the bell jar and the STM-Xwin23 software program.

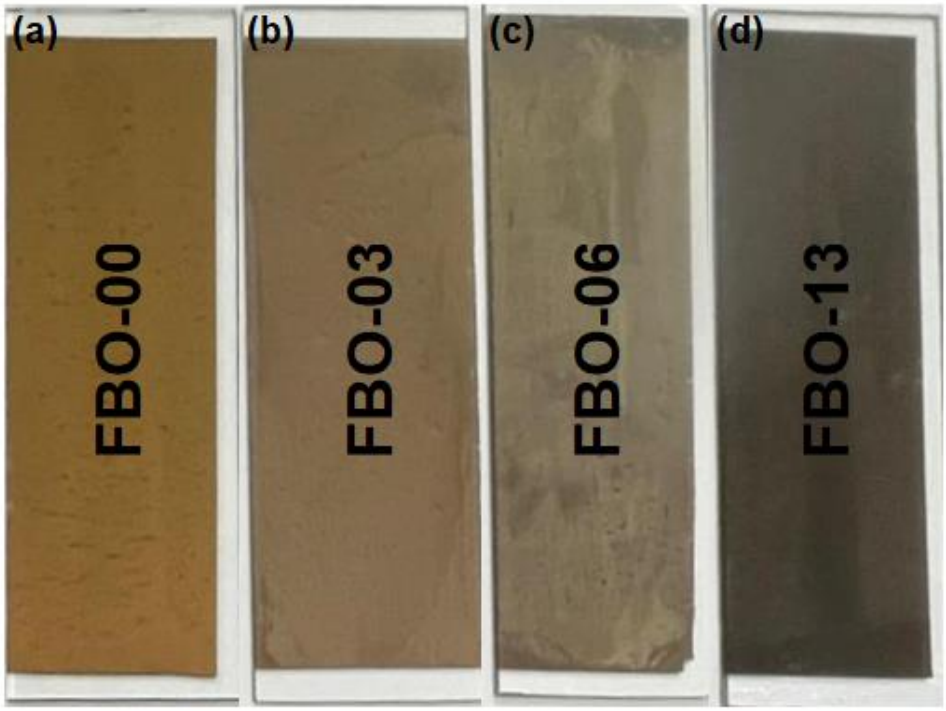

Figure 3.6. The optical images of the real samples.

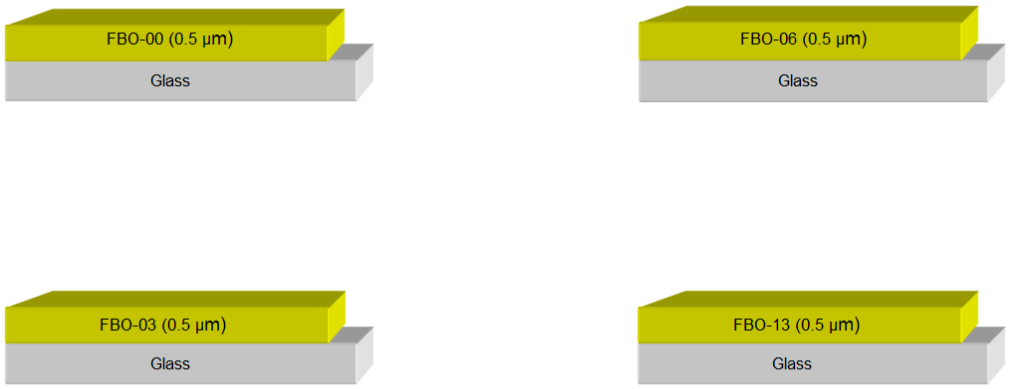

Figure 3.7. The geometrical design of the prepared films.

3.2 Thin film analysis

The fabricated films are subjected to the X-ray diffraction technique, scanning electron microscopy, energy dispersive X-ray spectroscopy and visible light spectrophotometry to explore the iron-doping effects on the structural, morphological, compositional and optical properties of bismuth oxide films.

3.2.1 The X-ray diffraction measurements

In order to study the structural properties, the pure and Fe-doped Bi_2O_3 films are subjected to the X-ray diffraction technique using the Rigaku Miniflex 600 X-ray diffractometer. The X-ray is generated inside the X-ray tube, filtered by a monochromator, collimated to concentrate, and directed toward the sample. Figure 3.8 displays the X-ray diffractometer with K_α radiation of a copper anode emitting X-ray with an average wavelength of 1.5418 Å at 40 kV and 15 mA. The diffractometer registered the intensity as a function of 2θ. The diffraction angle 2θ was set between $10^\circ - 80^\circ$, with a scan speed of $0.5^\circ/\text{min}$. Then, the MiniFlex support program connected with the x-ray diffractometer was used to collect the data. These data are

analyzed with the help of "Crystdiff" and "TREOR 92" software packages in order to determine the structural properties of these films. Figure 3.9 gives a deeper view of the X-ray diffractometer.

Figure 3.8. The Rigaku MiniFlex 600 X-ray diffractometer.

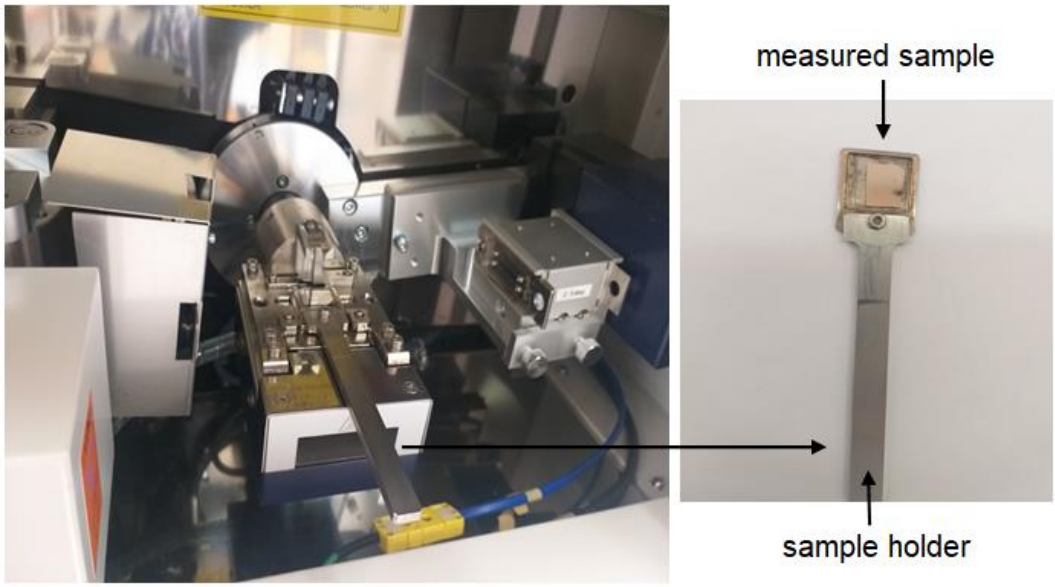

Figure 3.9. The components of the XRD main unit.

3.2.2 The morphological measurements

In order to study the morphological properties of the prepared films, the COXEM 200 scanning electron microscope (SEM) shown in Figure 3.10 was used. The SEM scans the surface of the film with a highly focused electron beam produced by an electron gun. These electrons interact with the atoms of the samples and create signals containing information about the composition of the studied sample. These signals include backscattered electrons, Auger electrons, X-rays, secondary electrons, etc. These secondary electrons are collected from each point of the sample using a secondary electron detector in order to display a 2D image that shows the morphological properties of the prepared film.

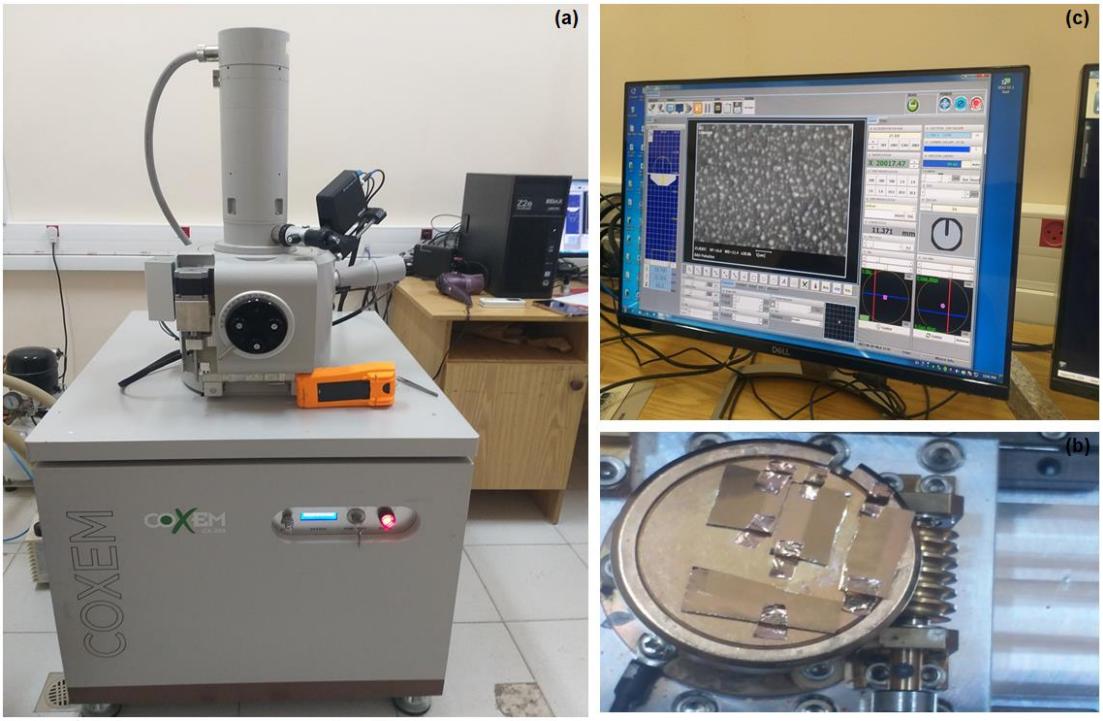

Figure 3.10. (a) The scaning electron microscope, (b) the samples hold in the microscope and (c) the imaging process of the microscope.

3.2.3 The compositional measurements

The energy dispersive X-ray spectroscopy technique (EDX) is used to determine the compositional properties of prepared samples. In this technique, the sample is bombarded by a high energy electron beam, and the electrons are excited from their inner shell to the outer shell, producing electron vacancies. Some electrons are transferred from the outer shell to the inner shell and release X-rays with energy equal to the energy between levels. Since the electron energy levels are quantized, the characteristic X-ray energy emitted by elements will often differ from one to another. If there is ambiguity in the determination of the peaks, the sample history will be used to identify the unknown beaks. Figure 3.11 displays the energy dispersive X-ray spectroscopy technique.

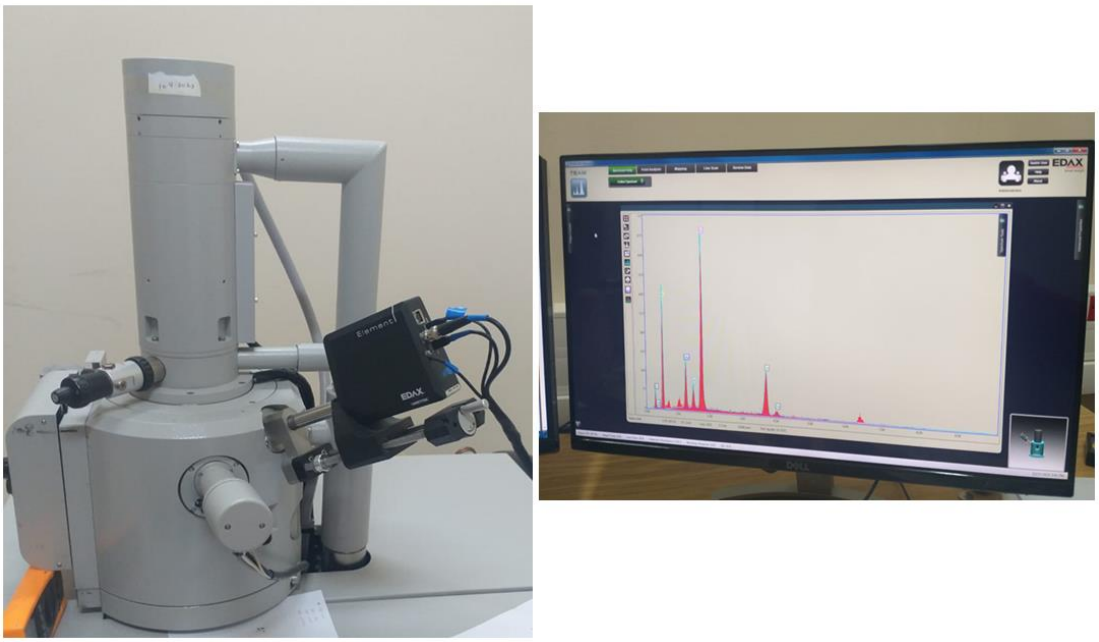

Figure 3.11. The energy dispersive X-ray spectroscopy.

3.2.4 The optical measurements

Figure 3.12 displays the Thermo Scientific Evolution 300 UV-Visible light spectrophotometer, which was used to explore the optical properties of fabricated thin films. The transmittance (T%) and reflectance (R%) spectral measurements were recorded in the range of wavelengths (190-1100 nm). The measurements were obtained at a scanning speed of 1200 nm/min. The data was collected and analyzed with the help of the Vision Pro software program that was attached to the system. The obtained data was used to calculate the absorption coefficient (α), band gap energies (E_g), band tail energies, and dielectric constant (ε).

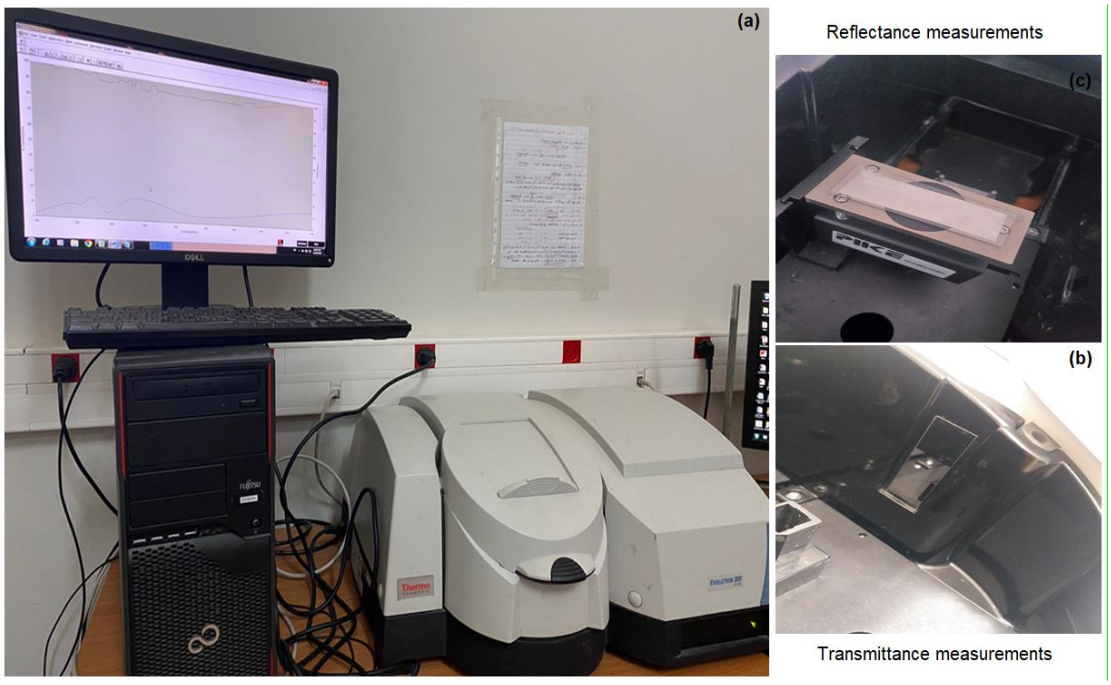

Figure 3.12. (a) The UV-VIS spectrophotometer, (b) the sample holder for transmittance measurement and (c) the reflectometer used to record the reflectance.

3.2.5 The hot probe technique

The hot probe technique is the simplest way to determine the conductivity type of semiconductors. This technique required a hot probe and a cold probe attached to the semiconductor surface. The hot probe is connected to the positive terminal of the digital multi-meter, while the cold probe is connected to the negative terminal. A simple explanation for the hot probe technique is that the majority of free carriers are moved from the hot probe to the cold probe within the semiconductor. The mechanism for this motion is a diffusion type. Therefore, when the voltage reading of the digital multi-meter is negative, the semiconductor is p-type. Whereas for an n-type semiconductor, a positive voltage is obtained. Figure 3.13 displays the set-up of this technique.

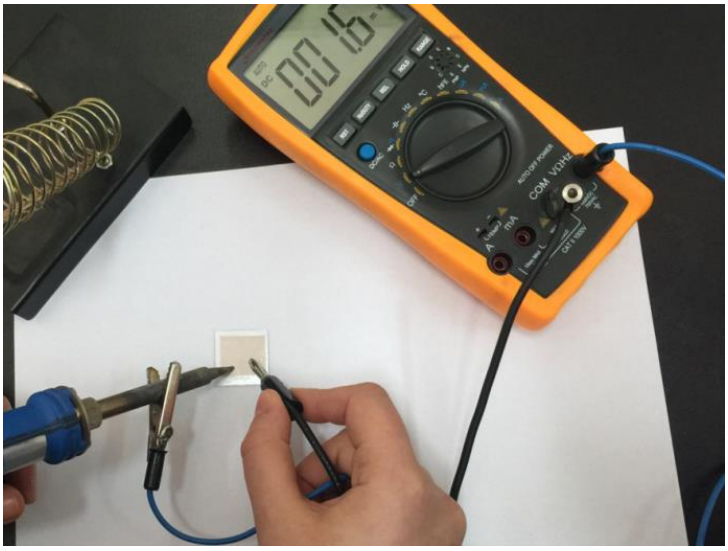

Figure 3.13. The set-up of the hot probe technique.

Chapter Four

Results and Discussions

This chapter explains the effects of iron doping on the structural, morphological, compositional, optical and dielectric properties of bismuth oxide films. The obtained results showed that iron enhanced the physical properties of bismuth oxide films.

4.1 Structural analysis

The optical images for pure and Fe-doped Bi_2O_3 thin films grown onto clean glass substrates by the thermal evaporation technique are shown in inset-1 of Figure 4.1. Pure Bi_2O_3 films displayed a bronze color. The colour of this sample is converted to tan, gray and black as the doping content increased from 3% to 6% and 13%, respectively. In order to explore the effect of the iron doping on the structural performance of bismuth oxide thin films, the X-ray diffraction patterns (XRD) of pure and Fe-doped Bi_2O_3 thin films are displayed in Figure 4.1. It is clear from Figure 4.1 that the pure Bi_2O_3 films $(FBO-00)$ exhibit a polycrystalline nature. The sharp XRD patterns are analyzed with the help of the "Crystdiff" and "TREOR 92" software packages. In the "Crystdiff" software packages, we inserted the XRD patterns of pure Bi_2O_3 films in order to determine the crystal structure and the miller indices for all diffraction peaks. The standard cards of cubic, tetragonal and monoclinic Bi_2O_3 such as JCPDS no. 27-0052, ICDD card no. 01-076-2477 and JCPDS card No. 14–0699 are compared to the observed XRD patterns. The observed experimental XRD patterns were not assignable to any card. Therefore, the "TREOR 92" software packages were used. In this software, we inserted the diffraction angles and intensity values and requested the solution that gives the lattice parameters and structure. The acceptable solution is the one that gives $\Delta\theta$ errors $(\theta_{observed}-\theta_{calculated})\times 100\%$ less than 5%. Several trials have been

conducted in order to explore the appropriate structure of the prepared films. Trials of cubic, hexagonal, trigonal, tetragonal and orthorhombic structures revealed errors larger than 5% for many observed diffraction patterns. So these solutions were rejected. On the other hand, the monoclinic structure revealed very small errors ($< 1\%$) compared to the other structures; therefore, this solution is accepted. The accepted solution was treated by the least squares method, and the miller indices for all peaks are interrupted in Table 4.1. The lattice parameter values for the monoclinic unit cell are found to be $a = 7.9765$ Å, $b = 7.1253$ Å, c $= 4.5964$ Å and $\beta = 102.203°$. It is clear that the crystalline planes are oriented in the (200) direction, as the maximum peak located at ($2\theta = 22.8°$) shows. This phase of bismuth oxide ($\alpha - Bi_2O_3$) was related to the $8/Lc140$ space group. The monoclinic phase of Bi_2O_3 is stable at room temperature [57].

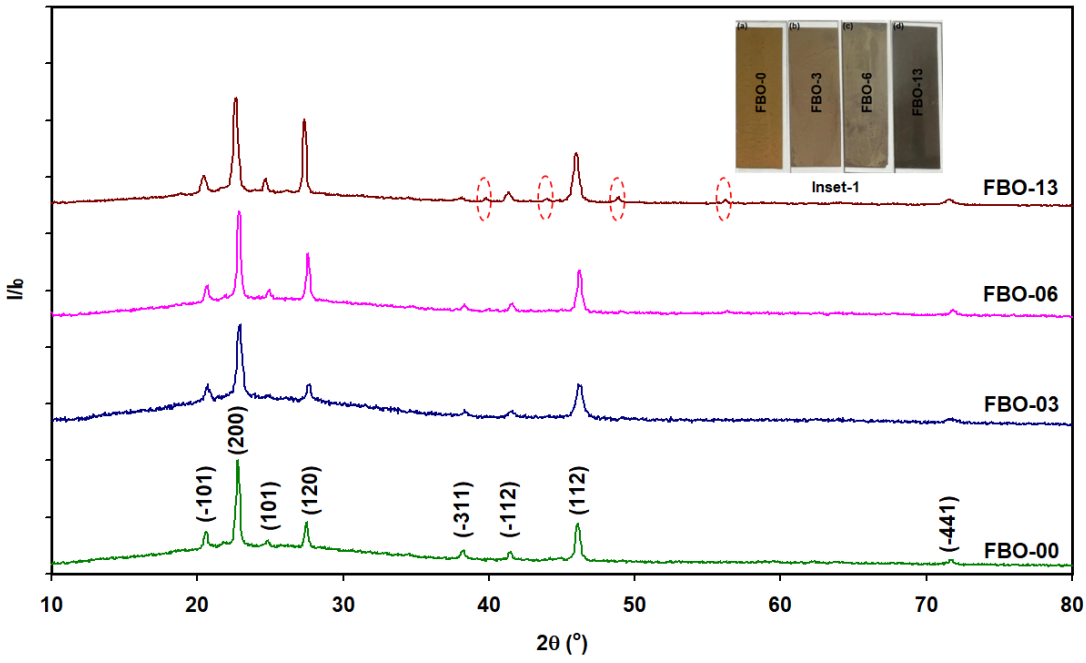

Figure 4.1. The X-ray diffraction patterns of the pure and Fe-doped Bi_2O_3 films. Inset-1 shows the optical images of the (a) $FBO-00$, (b) $FBO-03$, (c) $FBO-06$ and (d) $FBO-13$ samples.

Table 4.1. The miller indices assigned to the diffraction peaks for pure Bi_2O_3 films.

2θ (º)	I (a.u.)	(hkl)
20.60	**2108**	**(-101)**
22.80	**5600**	**(200)**
24.85	**1642**	**(101)**
27.50	**2566**	**(120)**
38.25	**1168**	**(-311)**
41.45	**1077**	**(-112)**
46.15	**2472**	**(112)**
71.80	**687**	**(-441)**

It is observed from Figure 4.1 that the XRD patterns of the doped samples exhibit nearly the same crystallization nature as pure Bi_2O_3 with some noticeable differences. Figure 4.2 gives deep information about the effects of iron doping on the structural performance of Bi_2O_3 films. It is clear from Figure 4.2 that the plastic deformations occur by introducing the first amount of dopants ($FB0-3$), since the shift in the maximum peak toward a larger diffraction angle is accompanied by a significant decrease in intensity [58]. Plastic deformation means a permanent deformation in the shape of solid material due to exceeding the elastic limit when an external force acts on it. By increasing the amount of dopants, the maximum peak became more intense and shifted systematically toward lower diffraction angles. The more intense peak means a larger number of oriented planes along a specific direction [59]. This was validated by calculating the degree of orientation, which raised from 0.29 for the $FBO-03$ samples to 0.31 for the $FBO-06$ samples. Then, this value decreased to 0.28 by increasing the doping content, as shown for the $FBO-13$ samples. This decrease indicates the formation of a new phase in the crystal structure of Bi_2O_3. It is worth noting that the iron oxide has many different phases, such as $Fe_{1-x}O$, Fe_3O_4, $\alpha-Fe_2O_3$ and $\gamma-Fe_2O_3$ [60]. It seems that the iron oxide makes a strong interaction when it interacts

with the material in sufficient quantity, as we observed for the $FBO-13$ sample. Therefore, it is not necessary for the pure and doped samples to behave systematically, since this depends on the amount of iron introduced to the pure sample and the iron oxide phase formed.

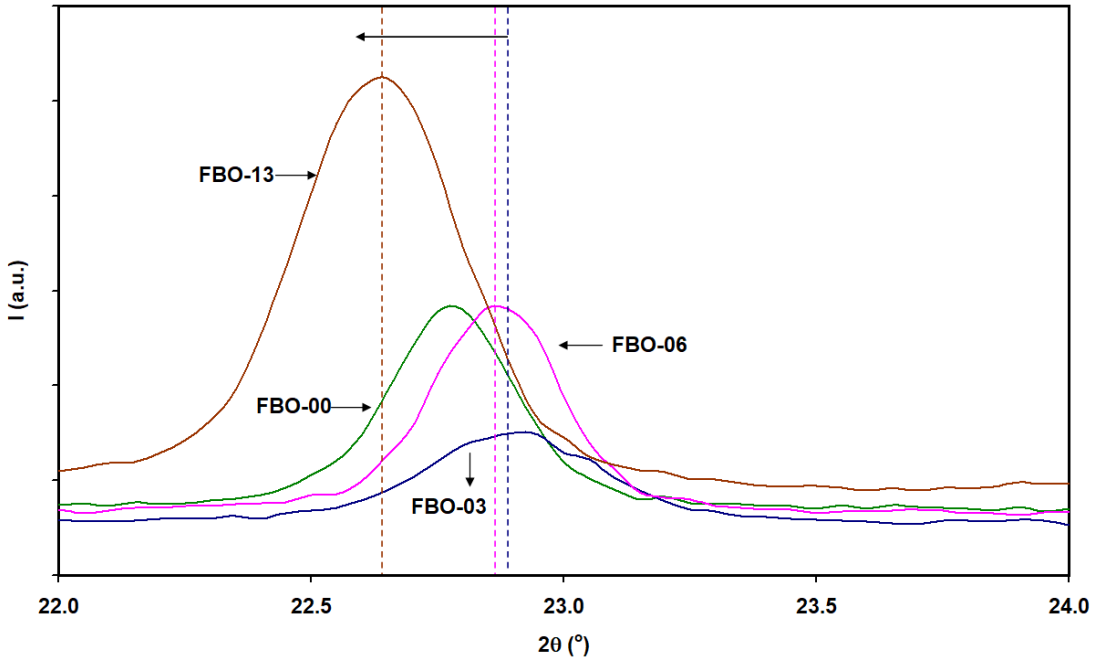

Figure 4.2. The shift in the maximum reflection peak of the Bi_2O_3 films as a function of Fe content.

It is worth noting that the XRD patterns of $FBO-13$ sample contained new diffraction patterns. These new patterns which are shown in red oval shape in Figure 4.1 and enlarged in Figure 4.3 are not related to the monoclinic phase of Bi_2O_3 according to the reflection list get from "TREOR 92" . The "Crystdiff" software packages confirmed that these additional patterns are related to orthorhombic Fe_2O_3 with lattice parameters $a = 5.072Å, b = 8.736$ Å, $c = 9.418$ Å and space group of $Pna2_1$ [61]. The appearance of Fe_2O_3 indicates that the doping level of 13% of the mass have reached the solubility limit. The orthorhombic Fe_2O_3 occupied 30.6% of the total phase of Bi_2O_3 films

according to the following equation ($\Delta\% = \frac{\sum A_{Fe_2O_3}}{\sum A_{\text{All peaks}}} 100\%$) [62], since $\Delta\%$ is the phase weight of Fe_2O_3 in Bi_2O_3 films and A is the area of the peak.

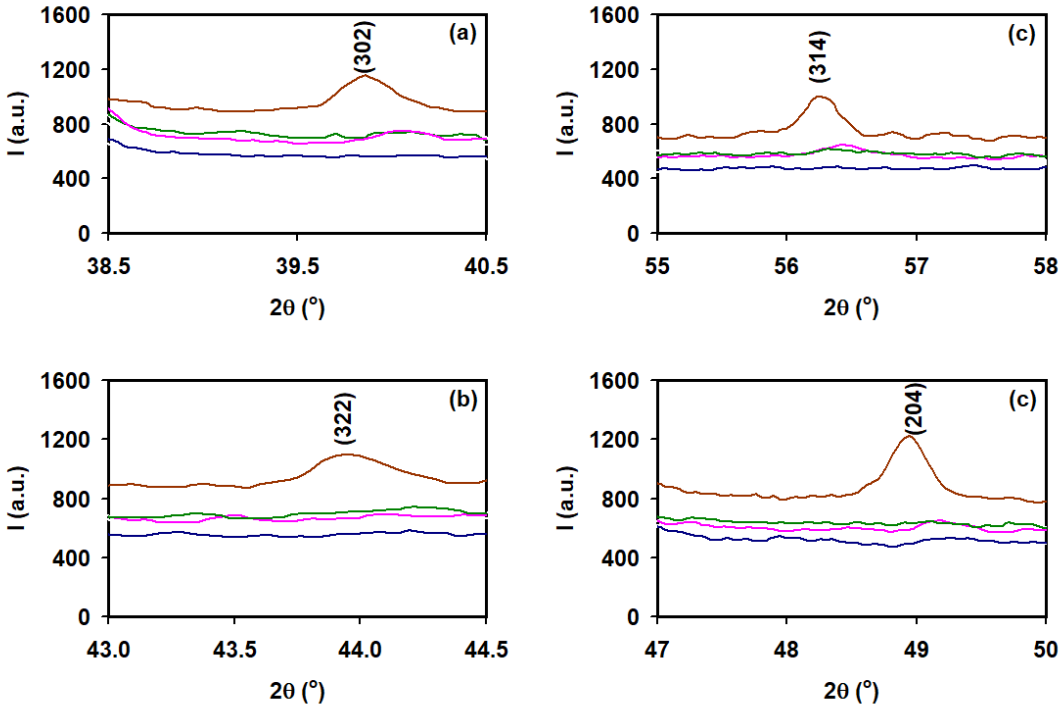

Figure 4.3. Showing the peaks of iron oxide in the XRD patterns for Bi_2O_3 doped with Fe of content of 13% with peaks observed at diffraction angles of (a) 39.8°, (b) 43.95°, (c) 48.95° and (c) 56.2°.

In order to understand the doping effects on the crystal structure, let us take all the constituents into consideration. We have bismuth (Bi), oxygen (O) and iron (Fe) atoms. The ionic radius of these atoms is tabulated in Table 4.2. The ionic radius of O^{2-} is reported to be 1.35 Å [63]. Also, it's clear that the ionic radius of Fe^{2+} (0.76 Å) and Fe^{3+} (0.64 Å) [64] is smaller than the ionic radius of Bi^{3+} (1.17 Å) [65]. Therefore, the substitution of Fe^{2+} or Fe^{3+} in the vacant sites of Bi^{3+} is preferable. This substitution motivates the formation of FeO or Fe_2O_3 bonds and clusters when exceeding solubility limit. The monoclinic phase of Bi_2O_3 ($\alpha - Bi_2O_3$) composed of eight bismuth atoms and twelve oxygen atoms in the unit cell [66]. This phase has Bi1 and Bi2 in addition to the three kinds of O atoms: O1, O2 and O3. Demonstration of the ($\alpha - Bi_2O_3$) phase

in addition to the bond length values are actualized with the help of "Crystal-Maker" software packages. The schematic diagram for the monoclinic phase of Bi_2O_3 is shown in Figure 4.4. The bond length values between neighboring atoms are displayed in Table 4.3. It is noticeable that the shortest bond is $O2 - O2$ (0.3848 Å) and the longest bond is $Bi2 - O1$ (1.9981 Å). Since the longest bond is the weakest bond, and the $Fe - O$ bond was reported to be 1.7873 Å [67], there is a high probability of interaction between iron and oxygen in the structure of Bi_2O_3.

Table 4.2. The ionic radius of iron, bismuth and oxygen ions.

Ion	**Fe^{2+}**	**Fe^{3+}**	**Bi^{3+}**	**O^{2-}**
Ionic radius (Å)	**0.76**	**0.64**	**1.17**	**1.35**

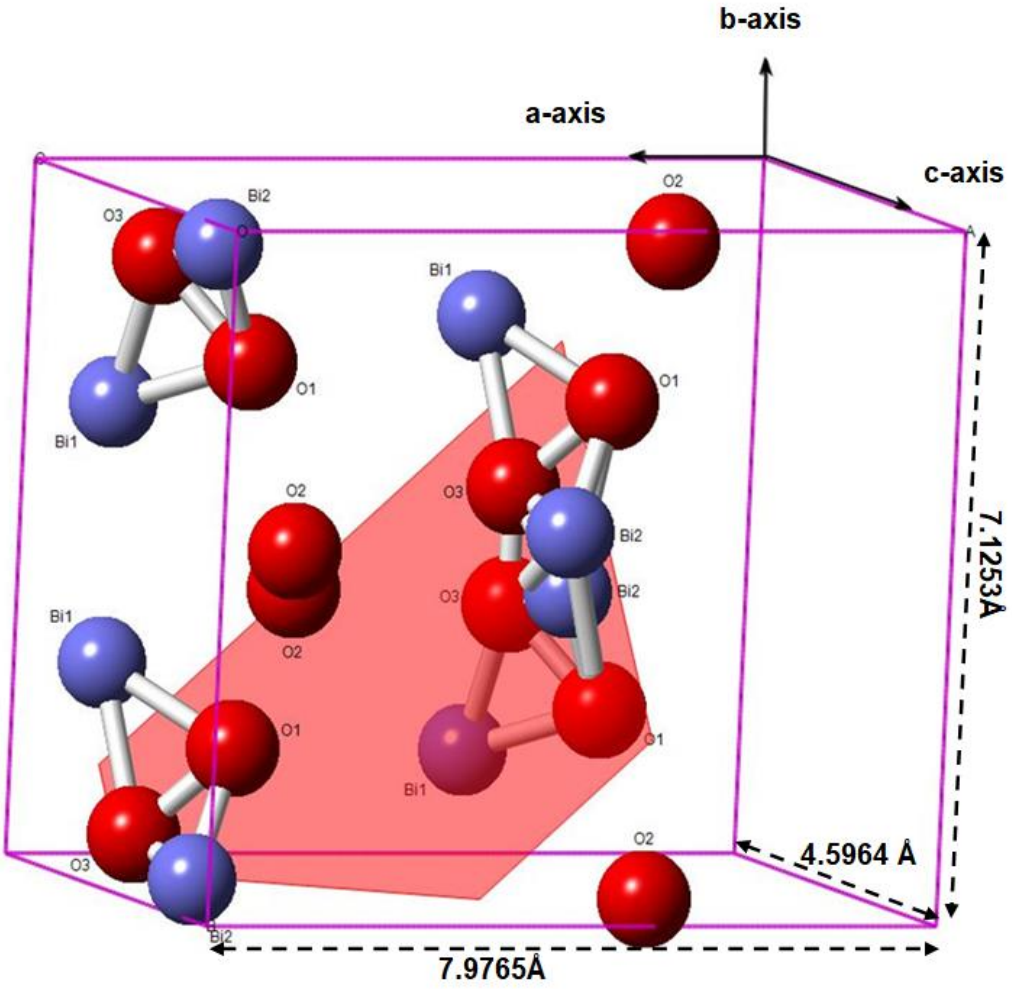

Figure 4.4. The schematic diagram of monoclinic bismuth oxide.

Table 4.3. The bond length of the bonding atoms.

Bond	Bond length (Å)
Bi1-O1	1.8999
Bi1-O3	1.8193
Bi2-O1	1.4331 1.9981
Bi2-O3	1.1518 1.4353
O1-O3	1.4611
O2-O2	0.3848
O3-O3	1.1971

The effect of the iron doping on the lattice parameters is almost negligible, since no change in the crystalline nature was observed, and the amount of deviation in the diffraction peaks is very small. Therefore, in this work, we will assume that the doping process did not have a significant impact on the lattice parameters. On the other hand, the inter-planer spacing (d), the crystallite size (D), micro-strain (ε), stacking faults (SF%) and defect density (δ) along the a,b and c-axes are calculated using the previous equations listed in chapter two. The calculated values of structural parameters for maximum intensity peaks are shown in Table 4.4.

Table 4.4. The structural parameters of pure and Fe-doped Bi_2O_3 thin films obtained from the main peak.

Sample	**FBO-00**	**FBO-03**	**FBO-06**	**FBO-13**
2θ (º)	22.80	22.90	22.85	22.65
I (a. u.)	5600	3011	5646	10485
d (Aº)	3.90	3.88	3.89	3.92
D (nm)	30	21	22	23
SF (%)	0.28	0.39	0.37	0.36
ε(x10^{-3})	6.06	8.62	8.20	8.06
$\delta_{a\text{-}axis}$ (x10^{11} lines/cm^2)	3.77	7.65	6.92	6.63
$\delta_{b\text{-}axis}$ (x10^{11} lines/cm^2)	4.22	8.57	7.75	7.42
$\delta_{c\text{-}axis}$ (x10^{11} lines/cm^2)	6.54	13.28	12.01	11.50
Degree of orientation	0.32	0.29	0.31	0.28

To get deep information about the affecting of structural parameters by the iron content, the effect of the iron doping on the crystalite size, on the micro-strain, on the stacking faults and on the defect density along the c-axis is presented in Figure 4.5 (a), (b), (c) and (d), respectively. It is clear from Figure 4.5 (a) that the crystalite size of doped samples decreased compared to the pure ones but was less sensitive to the Fe content. The decrease in crystalite size is associated with an increase in the micro-strain and defect density, as shown in Figure 4.5 (b) and (c), respectively.

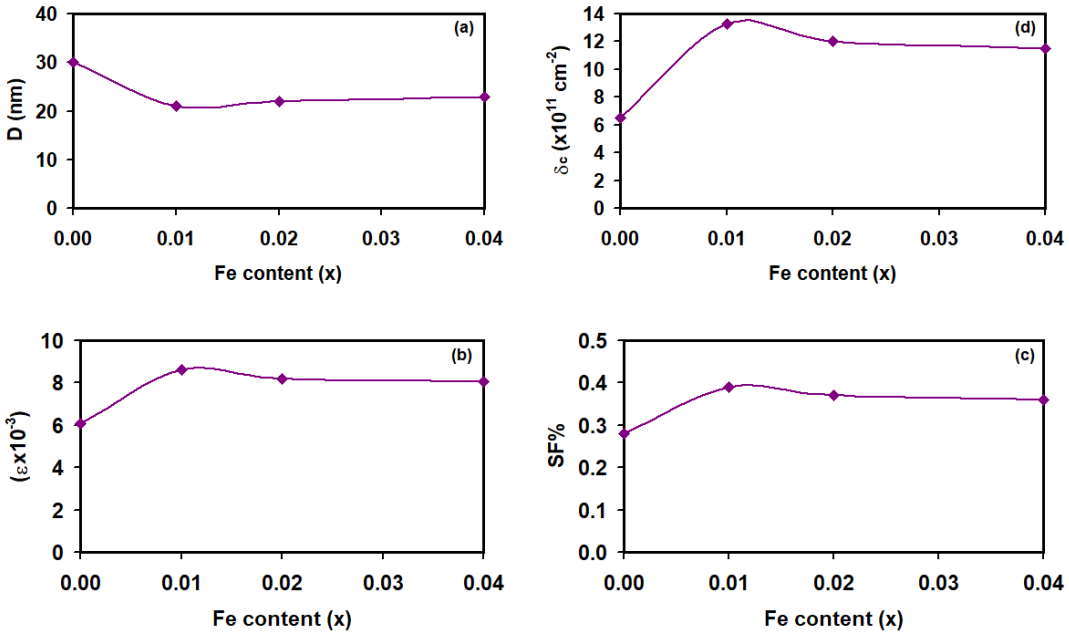

Figure 4.5. The dependencies of (a) the crystallite size, (b) the micro-strain, (c) the stacking faults and (d) the defect density along the c-axis on the Fe doping content for the Bi_2O_3.

Literature data included information about the preparation of doped Bi_2O_3 samples. It was reported that the maximum peak of Bi_2O_3 samples was shifted toward the lower diffraction angle when doped with Cu^{+2}. The shift in the maximum peak increased by increasing the amount of dopants [68]. On the other hand, it is worth noting that the grain size of pure Bi_2O_3 films decreased from 55nm to 25nm when doped with Sm^{+3}, then increased to 30 nm and 45nm by increasing the Sm^{+3} content [69].

4.2 Morphological analysis

The surface morphology of the prepared samples was tested with the help of a COXEM-200 scanning electron microscope. Figure 4.6 shows the SEM images for pure and Fe-doped samples being enlarged 10000 times of the original size recorded at 25 kV**.** Figure 4.6 (a) for pure Bi_2O_3 films indicates that the films exhibit a polycrystalline nature with dense grain distribution. The grains exhibit a circular shape with an average size of 200 nm. By introducing the first amount of dopants, tiny circular, non

systematically distributed grains of an average size of $280\ \text{nm}$ were observed, as shown in Figure 4.6 (b). For the $\text{FBO}-06$ sample, the SEM images reflect the formation of rectangular grains with an average size of $400\ \text{nm}$, as indicated in Figure 4.6 (c). Figure 4.6 (d) associated with the $\text{FBO}-13$ sample attracted attention, since it displayed two types of grains, rectangular and wires. The average size of rectangular grains was determined to be $520\ \text{nm}$. The average length and diameter of the wires were determined to be $1300\ \text{nm}$ and $200\ \text{nm}$, respectively. Such type of grains are always regarded as nanowires or nanowire bundles. The appearance of the nanowires in the $\text{FBO}-13$ samples is owed to formation of Fe_2O_3 clusters in the films [70]. The XRD analyses also shown the growth of Fe_2O_3 phase in FBO-13 samples. In general, it is clear that the grain sizes existing in doped samples increased with increasing doping concentration. The grain growth below the solubility limit is inherently attributed the atom diffusion resulting from smaller ionic radius of Fe^{+3} compared to Bi^{+3} as we discussed previously. Earlier studied on Fe doping effect on oxide materials have also reported shape and size changes of grains upon doping. The grain shape changed after doping due to the Fe^{+3} ionic substitutions affecting the charge carrier density and enhancing the polarity in addition to the increased potential energy of the specific crystal planes [71].

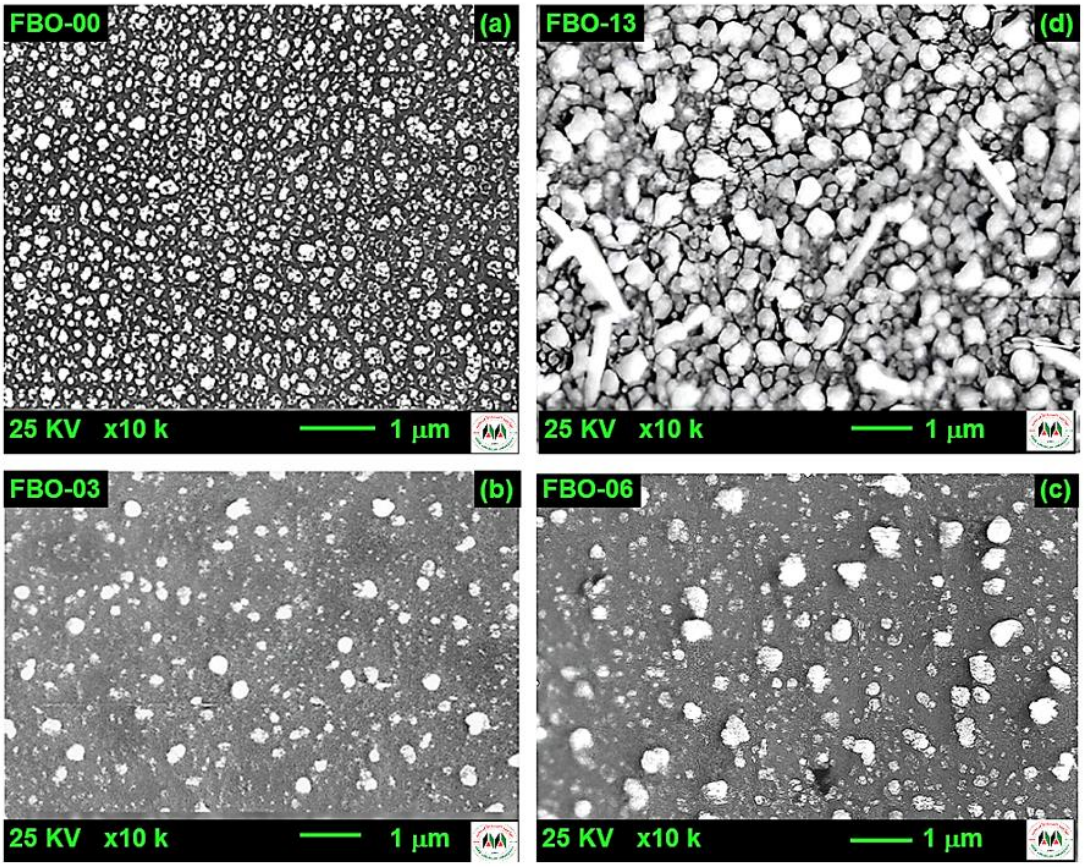

Figure 4.6. The scanning electron microscopy images for (a) FBO − 00, (b) FBO − 03, (c) FBO − 06 and (d) FBO − 13 samples.

4.3 Compositional analysis

In order to explore the atomic content of iron in the bismuth oxide, the pure and some Fe-doped Bi_2O_3 films were subjected to the energy dispersive X-ray spectroscopy technique (EDX). The EDX spectra of the FBO − 03 and FBO − 06 samples are shown in Figure 4.7. The EDX spectra of the studied films indicate the presence of glass $(SiO_2: Na_2O: MgO: CaO)$, Au, Fe, Bi and O atoms. No other impurities were detected. Au appears because the samples were coated with Au to prevent electron contamination. Because oxygen is one of the elements that is difficult to measure and is also present in the components of glass, it is therefore difficult for us to determine the accurate chemical formula of the compound formed. Hence, in this study, we will focus on the iron atomic content as indicated in inset-1 of Figure 4.7. For doped samples, it is clear

that the iron atomic content increases by increasing the amount of dopants. For example, the iron atomic content increases from $0.41\ \text{at.}\%$ for $\text{FBO}-03$ to $0.57\ \text{at.}\%$ and $0.96\ \text{at.}\%$ for $\text{FBO}-06$ and $\text{FBO}-13$ samples, respectively.

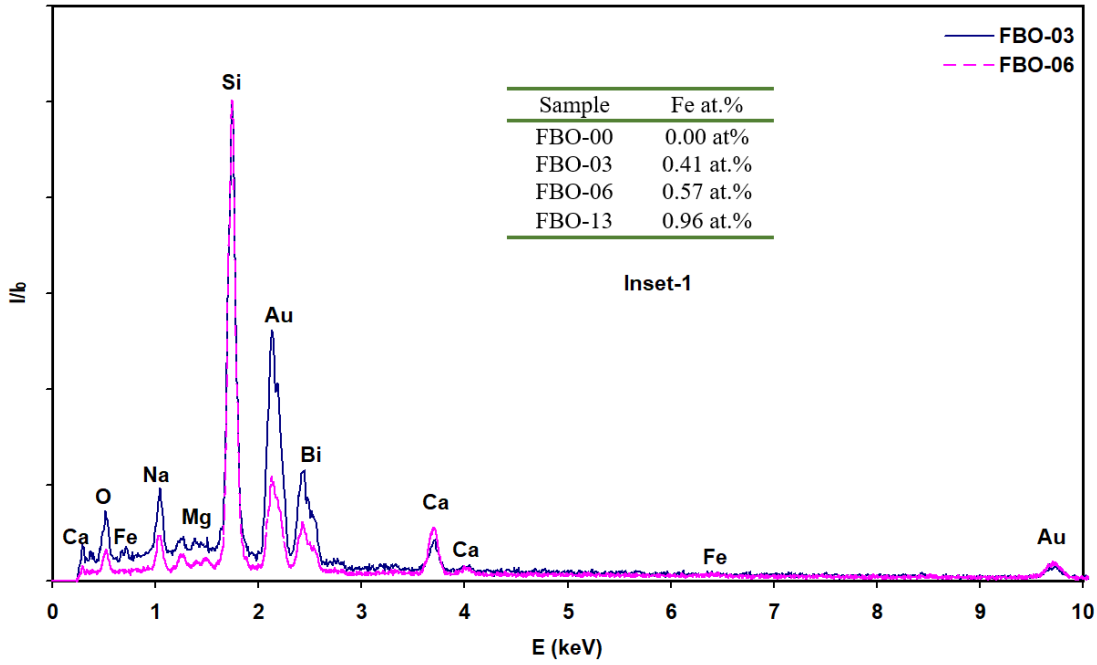

Figure 4.7. The energy dispersive X-ray spectra for some doped samples. Inset-1 shows the atomic content of iron in the measured samples.

4.4 Optical analysis

To explore the effect of the iron doping on the optical performance of Bi_2O_3 thin films, the transmittance (T%) and reflectance (R%) spectra for undoped and iron-doped samples were measured in the incident photon energy range $(1.13 - 4.5\ \text{eV})$. Both the fundamental optical parameters (T%) and (R%) are shown in Figures 4.8 and 4.9, respectively. It is clear from Figure 4.8 that the $\text{FBO}-00$ sample exhibits a maximum transmittance value of 12% at $1.13\ \text{eV}$. The transmittance spectrum of this sample hardly changes in the energy range of $(1.13 - 3.5\ \text{eV})$. The transmittance spectrum starts to decrease from the beginning of UV range ($3.3\ \text{eV}$) until it reaches nearly 0% in the range of light $(4.1 - 4.5\ \text{eV})$. For doped samples, the maximum transmittance

value that was observed at 1.13 eV was increased slightly to exhibit values in the range of $(14\% - 16\%)$. In the ultraviolet range of light, it was observed that the transmittance behavior of the doped samples is very similar to that of the pure samples, since the transmittance began to decrease at 3.3 eV. It is clear from Figure 4.8 that the doping content does not have a significant impact on the transmittance values since the differences between doped samples are nearly unnoticeable. The main reason beyond the higher transparency of doped samples compared to the pure samples is the presence of iron oxide phase in the bismuth oxide phase [72]. For example, the phase weight of Fe_2O_3 in $FBO - 13$ samples was calculated to be 30.6% as we discussed previously.

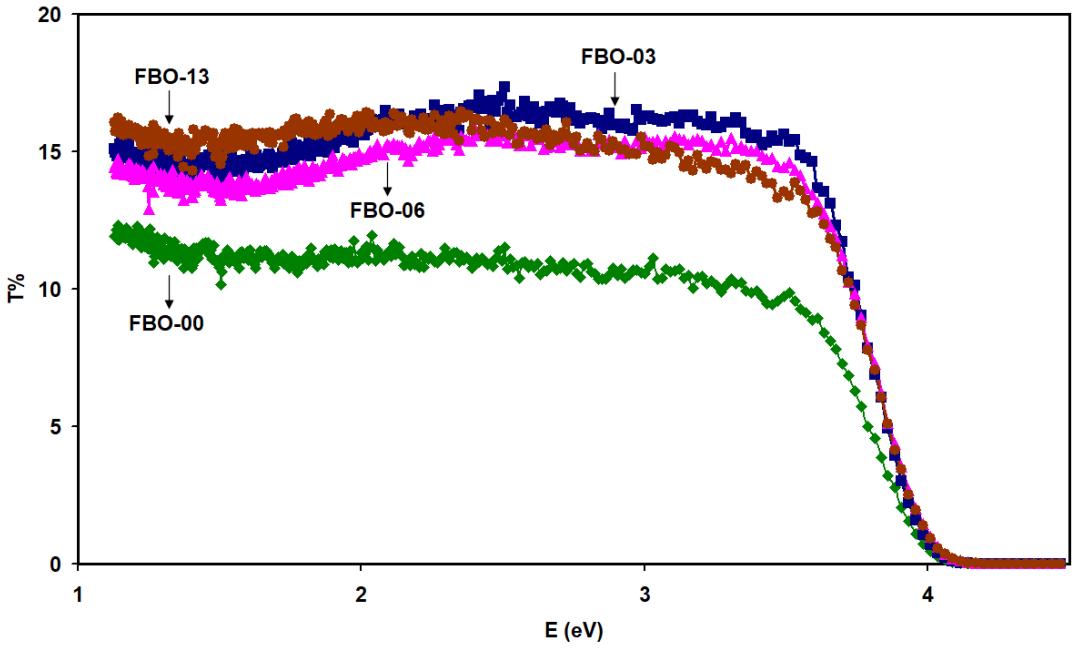

Figure 4.8. The transmittance spectra for the pure Bi_2O_3 and Fe-doped Bi_2O_3 samples.

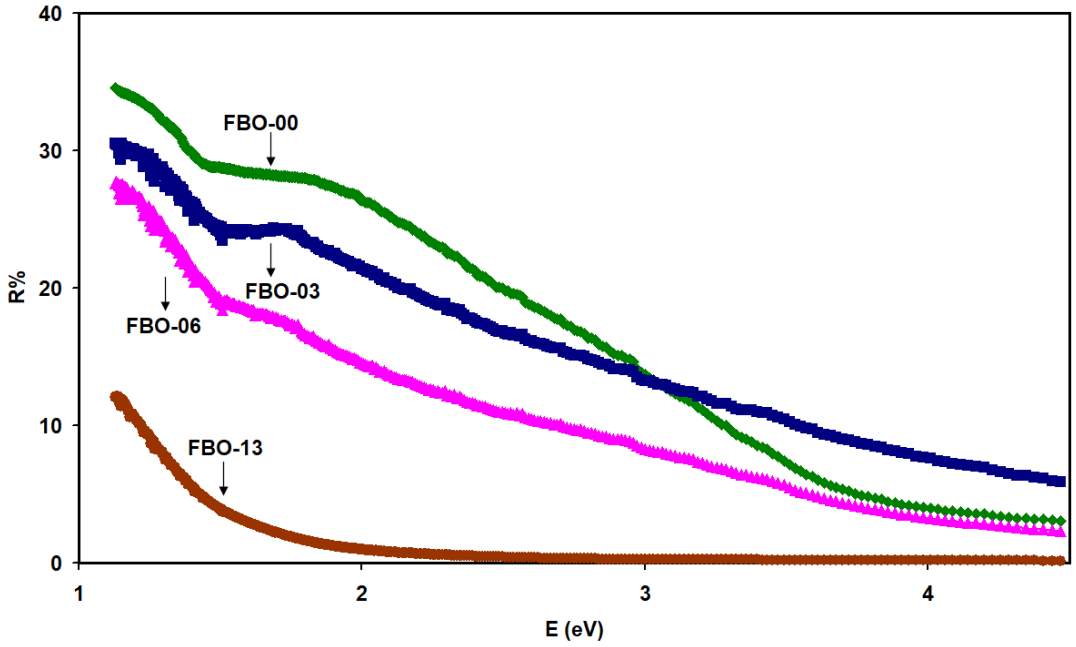

Figure 4.9. The reflectance spectra for the pure Bi_2O_3 and Fe-doped Bi_2O_3 samples.

The reflectance spectra for the undoped and doped samples are shown in Figure 4.9. It is noticeable that the reflectance spectra for all samples are decreasing with increasing incident photon energy in the range of $(1.13 - 1.53\ eV)$. At $1.53\ eV$, the reflectance spectra for the $FBO - 00$ and $FBO - 03$ samples change the trend of variation and exhibit nearly constant values in the energy range of $(1.53 - 1.75\ eV)$. By increasing the iron content, this behavior disappeared. In the range of $(1.75 - 4.5\ eV)$, it is clear that the reflectance spectra for $FBO - 00$, $FBO - 03$, and $FBO - 06$ samples decrease with increasing incident photon energy. The reflectance spectra for the $FBO - 00$ and $FBO - 03$ samples intersect at $3.10\ eV$, and the reflectance spectra for the $FBO - 03$ sample exhibit higher values than those of the $FBO - 00$ sample. For the $FBO - 13$ sample, the reflectance spectrum displays an almost constant region in the range of $(2.5 - 4.5\ eV)$. The higher reflectance values for these films enable us to use them as high k-gate dielectrics. The reflectance decreased with increasing Fe content due to the

constitution of optically active sub-levels within the band gap that are formed by increased doping content [73].

It is evident from Figures 4.8 and 4.9 that $T\% + R\% \neq 100\%$ in all measured spectral ranges. This indicates that light absorption is still dominant. Hence, Figure 4.10 demonstrates the absorption coefficient (α) spectra for all measured samples. The $\alpha - E$ spectra, which are determined by the previously described equation (2.29), display three regions of absorption. The first region is the sharp absorption region in the range of $(3.6 - 4.2\ \text{eV})$. In this region, the absorption coefficient is sharply decreasing with decreasing incident photon energy. In the second region $(1.4 - 3.6\ \text{eV})$, the absorption coefficient spectra follow a different trend of variation compared to that of the first region. The α spectra for all samples are nearly constant. The constant value of the absorption coefficient in this wide range is an advantage, since it means constant internal quantum efficiency and constant responsivity in the studied spectral range [66]. In the lowest absorption region $(1.13 - 1.4\ \text{eV})$, the α spectra of the prepared samples showed a slow, decreasing trend of variation with decreasing incident photon energy. This observation about decreasing the α spectra by decreasing the incident photon energy in the lower energy range gives evidence about the formation of the band tails and/or interbands in the studied films. The band tails in semiconductors are often formed by inhomogeneities, impurities, defects, and broken bonds [74]. The existence of interbands in Bi_2O_3 films is associated with the transitions between the defects and different valence states in Bi ions (Bi^{+2} and Bi^{+3}) [75]. In general, the absorption coefficient spectra of Fe-doped Bi_2O_3 samples are lower than those of pure Bi_2O_3 samples. This behavior is due to the interaction between iron and oxygen in Bi_2O_3. The absorption levels in Fe_2O_3 are lower than those of Bi_2O_3 leading to a decrease in α values [76].

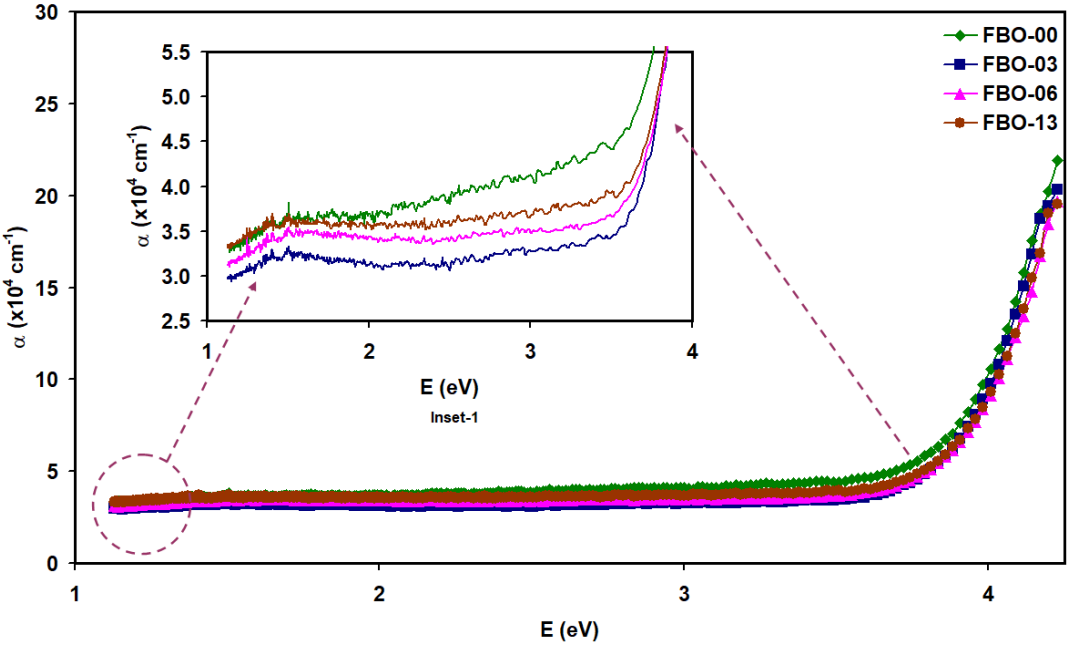

Figure 4.10. The absorption coefficient spectra for the pure Bi_2O_3 and Fe-doped Bi_2O_3 samples.

Figure 4.11 illustrates the fitting of Tauc's equation for the absorption coefficient spectra in the sharp absorption region in order to explore the effect of the doping process on the optical energy band gap. With the help of Tauc's equation (2.30), the most appropriate fit is found to be $p = \frac{1}{2}$. Therefore, the plotting of $(\alpha E)^2 - E$ is used to calculate the optical energy band gap since the intercept of the $E -$ axis represents the values of direct allowed energy bands. The energy gap value for the $FBO - 00$ sample was recorded to be 1.60 eV. By introducing the iron dopants on the Bi_2O_3 samples, the band gap energy decreased to 1.55 eV, 1.50 eV and 1.46 eV for the $FBO - 03$, $FBO - 06$ and $FBO - 13$ samples, respectively.

The valence band of bismuth oxide is composed of $O(2p)$ states and the conduction band is formed from $Bi(6p)$ states [77]. The doping of iron leads to a band position different from the original one. The addition of iron with the electronic configuration $Fe(3d^6 4s^2)$ which is at lower 3d states than $Bi(4f^{14}5d^{10}6s^2 6p^3)$. $5d^{10}$ strongly

influences the valance band edge due to the interaction of oxygen with iron. The inability of Fe to reach conduction band states (5d) of Bi_2O_3 indicates the possible formation of impurity bands in the band gap, causing the observed decrease in energy gap value [78]. Another reason is due to the shifting of the conduction band minimum and valance band maximum of the material [79].

It is worth noting that the narrowing of the optical energy gap with increasing dopant content was also observed in the Fe doped TiO_2 nanocrystal [80]. The most important explanation for the band gap narrowing in Fe doped TiO_2 is the creation of surface trap centers by oxygen vacancy defect sites of Fe^{+2} / Fe^{+3} and Ti^{+3} or sp-d exchange interactions between Fe^{+2} / Fe^{+3} ions at Ti^{+4} sites. The same behavior was observed for Fe doped ZnO particles [81], it was found that the sp-d exchange interaction between the band electrons and the localized (d) electrons of the metal ion Fe^{+2} / Fe^{+3} substituting the cation Zn is responsible for the shranking of the optical energy gap. On the other hand, the narrowing of the energy gap is also observed in Sm^{+3} doped Bi_2O_3 photocatalyst, which was prepared by the hydrothermal method [69]. The redshift of the band gap energy was interpreted as a substitution of Sm^{+3} ions, this introduces new interband trap sites that capture the electrons excited from the valence band of bismuth oxide. The decrease in optical energy gap is very important in solar energy [82] and phosphor-converted white light emitting diode applications [83].

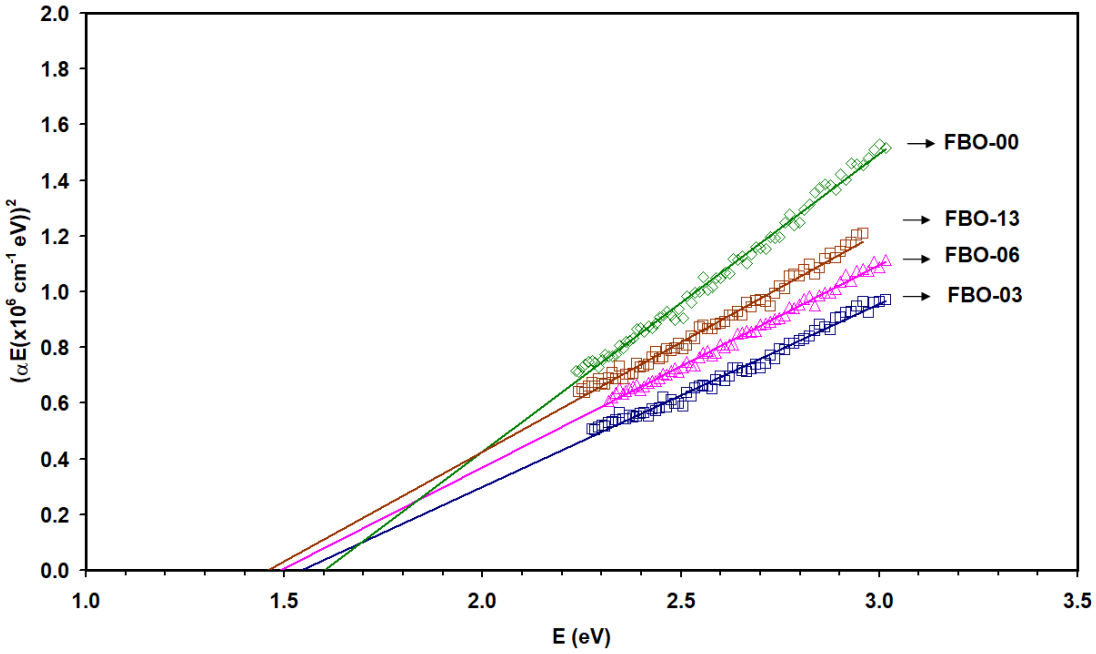

Figure 4.11. The $(\alpha E)^2 - E$ for the pure Bi_2O_3 and Fe doped Bi_2O_3 films in the sharp absorption region.

Returning back to the lowest absorption region, in which the absorption coefficient spectra decrease with decreasing incident photon energy. In order to determine the width of the energy band tail (E_e), the Urbach rule (2.31) was used. As shown in Figure 4.12, the plot of $\ln(\alpha) - E$ variation in the lower energy range $(1.13 - 1.4\ eV)$ gives a straight line for all prepared samples. It is clear that the straight line associated with the prepared samples is decreasing slowly by decreasing the incident photon energy, as we discussed previously. The energy band tail (E_e) values were determined from the reciprocal of the linear slope of the $\ln(\alpha) - E$ plot. These values were calculated to be $2.86\ eV,\ 3.37\ eV,\ 3.12\ eV$ and $3.46\ eV$ for $FBO-00,\ FBO-03,\ FBO-06$ and $FBO-13$ samples, respectively. But the band tail should be within the energy band gap. This means that $E_e < \frac{Eg}{2}$. The calculated values suggested that the tail width energy is greater than half of the energy band gap, which up to our knowledge means that there are no band tails.

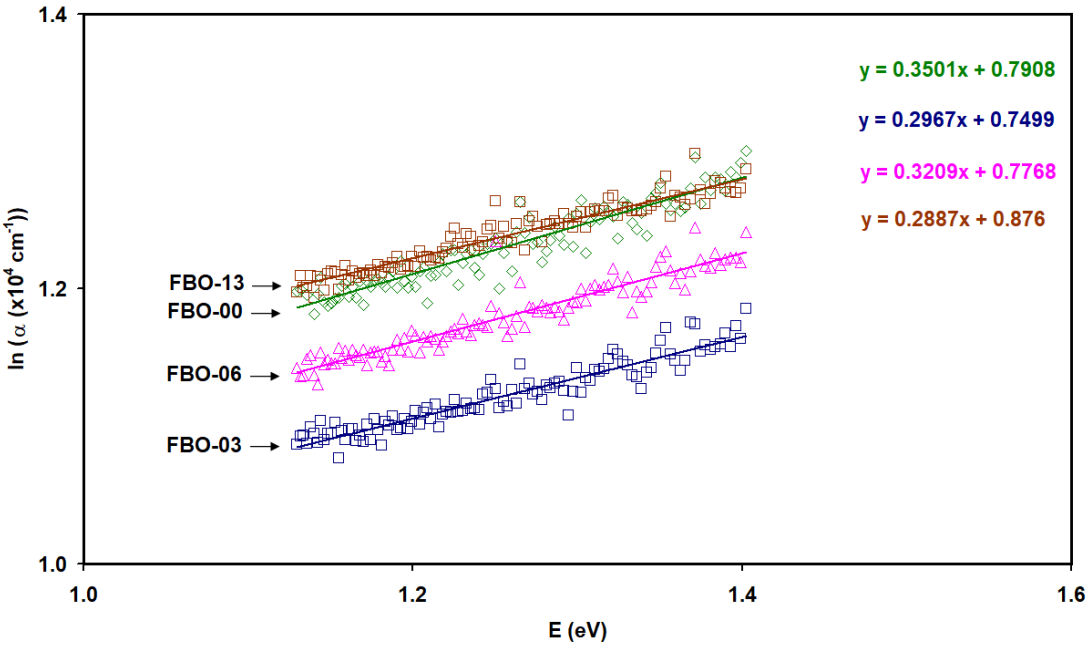

Figure 4.12. The $\ln(\alpha) - \mathrm{E}$ for the pure Bi_2O_3 and Fe-doped Bi_2O_3 films in the lowest absorption region.

To find practical applications for iron-doped bismuth oxide samples, the dielectric spectra were calculated using reflection and absorption coefficient spectral data with the help of Fresnel's equations. The real part (ε_r) of the dielectric constant spectra as a function of incident photon energy for the undoped and iron-doped samples are displayed in Figure 4.13. It is clear from the Figure that the real part of the dielectric constant spectra exhibit systematic behavior by increasing the amount of dopants. It is clear from the Figure that the real part of the dielectric constant for all samples sharply increases by decreasing the incident photon energy in the infrared range of light ($1.13 - 1.5$ eV). The increase in the real part of the dielectric constant with decreasing incident photon energy provides information about the capacitance spectra [75]. Since $C = \frac{\varepsilon_r A}{x}$ where ε_r is the real part of the dielectric constant, x is the depletion width, and A is the area. The increase in capacitance values due to the increase in the dielectric constant in the infrared range of light means possible applications in wireless communications technology in the terahertz frequency domain [75]. On the other hand, the increase in

the real part of the dielectric constant in the infrared range of light is an advantage since the electro-optical attenuation coefficient and the amplification factor of an electromagnetic radiation detector increase with increasing dielectric constant values [66]. In the energy range of $(1.74 - 4.25\ \text{eV})$, Although the dielectric constant for the $\text{FBO} - 00$, $\text{FBO} - 03$, and $\text{FBO} - 06$ samples continuously increases with decreasing incident photon energy, the real part of the dielectric constant spectra for the $\text{FBO} - 13$ very slowly increases. Generally, the higher values of the dielectric constant of the prepared samples make them important for use as high k-gate dielectrics, which play an important role in complementary metal oxide semiconductor integrated circuits, transistors and storage capacitors [84].

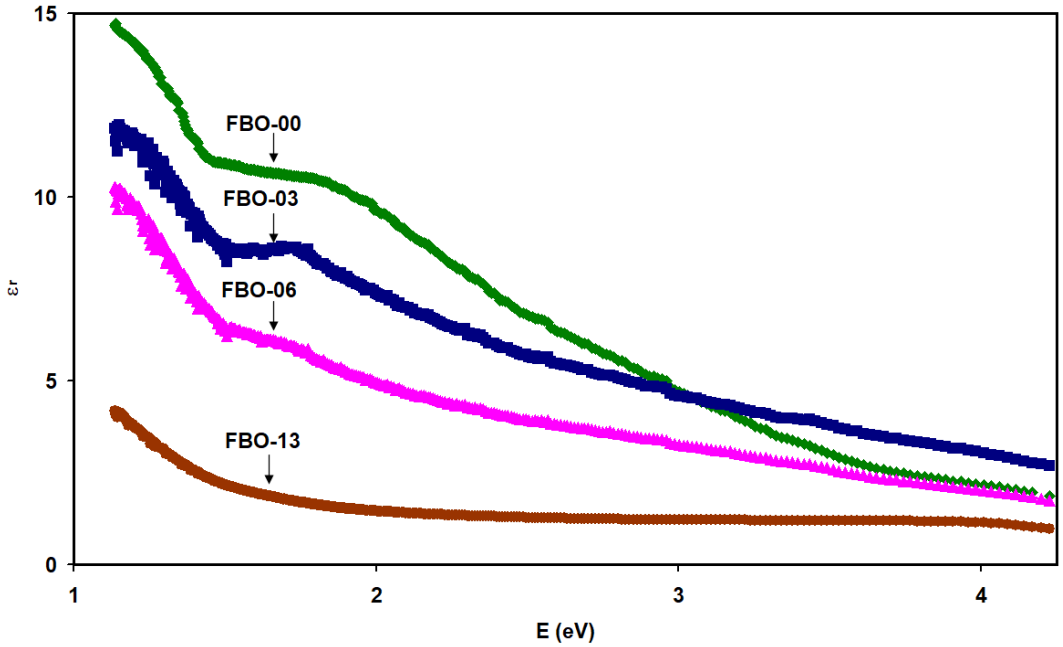

Figure 4.13. The real part of the dielectric spectra for the pure Bi_2O_3 and Fe-doped Bi_2O_3 films.

On the other hand, the imaginary part of the dielectric constant as a function of incident photon energy is shown in Figure 4.14. It is clear that the imaginary part of the dielectric constant for all samples follows nearly the same trend of variation as that of the real part but with lowered values. Also, it is observed that the imaginary part of the dielectric

constant is increasing with increasing incident photon energy in the UV range of light ($3.90 - 4.25$ eV).

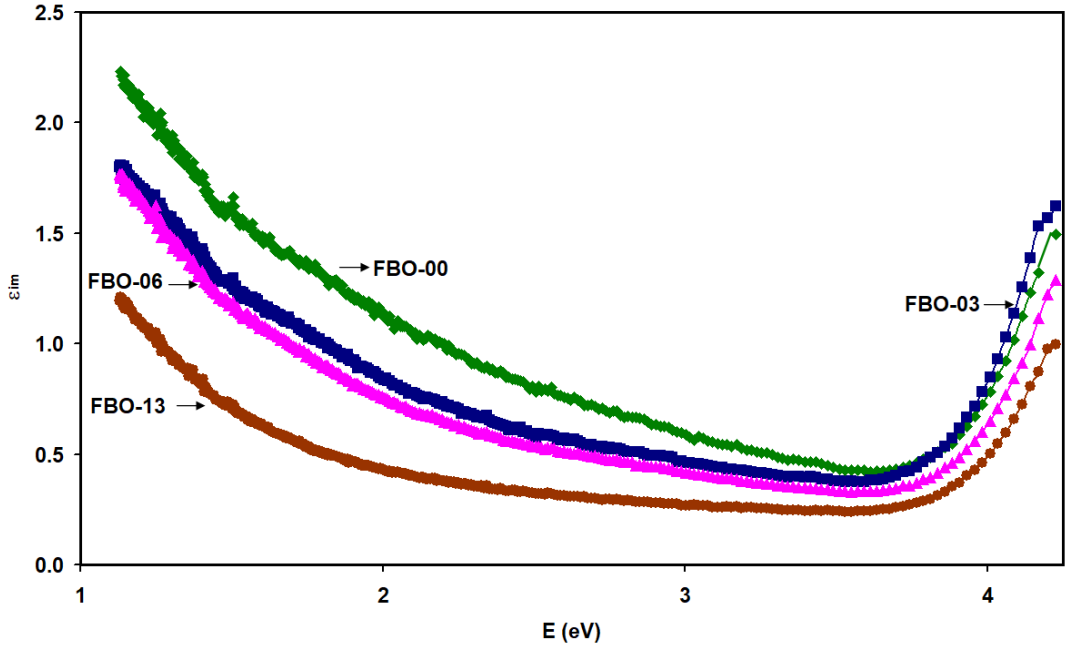

Figure 4.14. The imaginary part of the dielectric spectra for the pure Bi_2O_3 and Fe-doped Bi_2O_3 films.

To get deep information, the imaginary part of the dielectric constant spectra is modeled according to the Drude-Lorentz model through the modeling relation [85].

$$\varepsilon_{im} = \sum_{i=1}^{k} \frac{w_{pei}^2 \, w}{\tau_i((w_{ei}^2 - w^2)^2 + w^2 \, \tau_i^{-2})} \tag{4.1}$$

Where, k is the number of dominant linear oscillators, $w_{pe} = \sqrt{4\pi n e^2/m^*}$ is the electron bounded Plasmon frequency, $w = 2\pi f$ is the angular frequency of the incident light, w_e is the reduced resonant frequency, τ is the average scattering time and represents the inverse of the damping coefficient. m^* is the free carrier effective mass and n is the free electron density. The free-carrier mobility is also determined by the formula $\mu = e\tau/m^*$. Since all the prepared samples exhibit n-type conductivity according to the hot probe technique, the effective mass for electrons in Bi_2O_3 ($m^*_{Bi_2O_3}$)

was reported to be $0.68\, m_o$ [86] and assuming an electron effective mass of $1m_o$ for Fe metal. Then the reduced mass for the Fe-doped Bi_2O_3 is 0.405 m_o according to the following relation: $(m^*{}_{Fe\ doped\ Bi_2O_3} = [(m^*_{Fe})^{-1} + (m^*_{Bi_2O_3})^{-1}]^{-1})$. The fitting of the imaginary part equation assuming the presence of five oscillators (k = 5) is shown by the dark color in Figure 4.15. Good correlation between the theoretical and experimental spectral data was obtained via the fitting parameters, which are calculated and tabulated as indicated in Table 4.5.

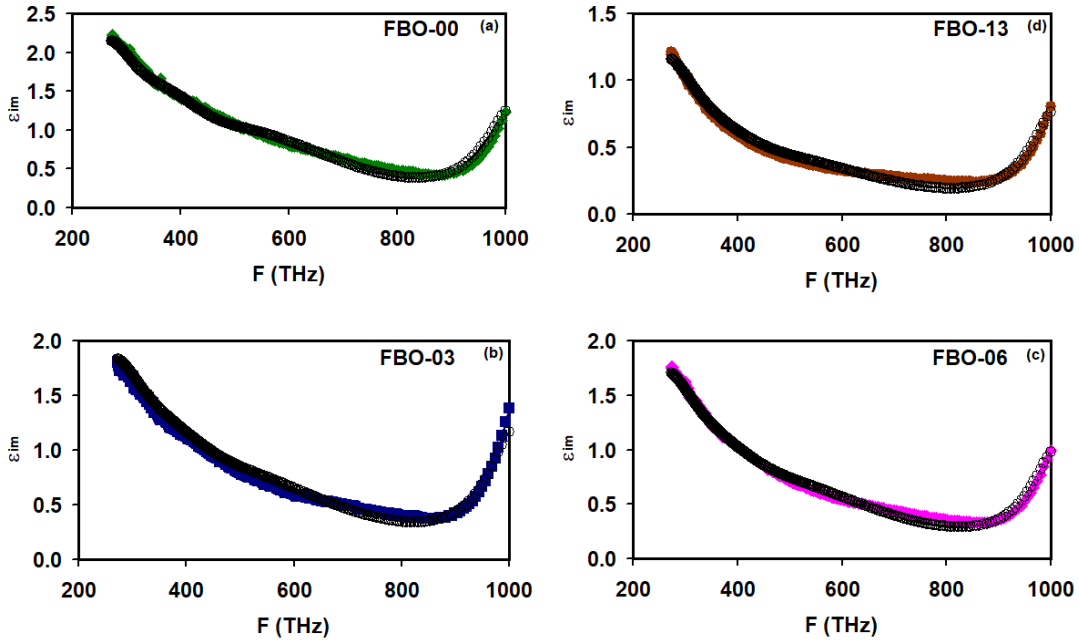

Figure 4.15. The imaginary part of the dielectric constant spectra fitted according to the Drude-Lorentz model.

Table 4.5. The optical conductivity parameters for (a) FBO − 00, (b) FBO − 03, (c) FBO − 06 and (d) FBO − 13 samples.

(a) FBO − 00

K_i	1	2	3	4	5
τ(fs)	1.0	0.7	0.6	0.5	1.2
E_e (eV)	1.12	1.64	2.30	2.76	4.20
n ($x10^{18}$ cm^{-3})	48.0	47.0	40.0	39.0	110.0
ω_p (GHz)	4.99	4.94	4.56	4.50	7.56
μ (cm^2/Vs)	2.59	1.81	1.55	1.29	3.10

(b) FBO − 03

K_i	1	2	3	4	5
τ(fs)	0.9	0.6	0.5	0.4	1.2
E_e (eV)	1.12	1.64	2.30	2.76	4.20
n ($x10^{18}$ cm^{-3})	26.0	23.0	19.0	18.0	60.0
ω_p (GHz)	4.82	4.54	4.12	4.01	7.33
μ (cm^2/Vs)	4.01	2.67	2.23	1.78	5.35

(c) FBO − 06

K_i	1	2	3	4	5
τ(fs)	0.9	0.6	0.5	0.4	1.2
E_e (eV)	1.12	1.64	2.30	2.76	4.20
n ($x10^{18}$ cm^{-3})	25.0	19.0	17.0	15.0	50.0
ω_p (GHz)	4.73	4.12	3.90	3.66	6.69
μ (cm^2/Vs)	4.01	2.67	2.23	1.78	5.35

(d) FBO − 13

K_i	1	2	3	4	5
τ(fs)	0.9	0.6	0.5	0.4	1.2
E_e (eV)	1.12	1.64	2.30	2.76	4.20
n ($x10^{18}$ cm^{-3})	18.0	10.0	10.0	9.0	40.0
ω_p (GHz)	4.01	2.99	2.99	2.84	5.98
μ (cm^2/Vs)	4.01	2.67	2.23	1.78	5.35

It is clear from the tabulated data that there exist two infrared oscillators dominant in the infrared range of light $(1.12 \text{ and } 1.64 \text{ eV})$, two oscillators in the visible range of light $(2.30 \text{ and } 2.76 \text{ eV})$ and one UV oscillator centered at 4.2 eV. Also, it is evident from the Table that regardless of the doping level, the electron-Plasmon coupled oscillator energies are the same. The damping coefficient which is defined as the inverse of the scattering time constant is also invariant with doping content. Such property also applies for the drift mobility of the samples under study. However, remarkable effect of doping content is observed on the free electron concentration. Namely, the free electron concentrations and the Plasmon frequency accordingly decreased with increasing iron content. It decreased from $4.8 \times 10^{19}\ cm^{-3}$ to $2.6 \times 10^{19}\ cm^{-3}$ and reaches $1.8 \times 10^{19}\ cm^{-3}$ as the doping content increases from 0 wt. % to 3.0 wt. % and reaches 13.0 wt. % . The decrease in the free electron concentrations with increasing doping content is ascribed to the substitution of iron in sites of bismuth. The electronic configuration of iron is at lower orbital energies than bismuth leading to less orbital overlapping. Hence, lower free electron concentration available for conduction [87]. It is also observed from Table 4.5 that the free electron mobility highest for UV oscillator and then for IR oscillator. It means that Bi_2O_3 are adequate for the fabrication of UV and IR sensors rather than visible light sensors.

The optical conductivity which is calculated from the imaginary part of the dielectric constant according to the equation $(\sigma(w) = \frac{w\varepsilon_{im}}{4\pi})$ is shown in Figure 4.16. In the energy range of $(1.12 - 3.72 \text{ eV})$, the optical conductivity spectra decreased slowly with increasing incident photon energy. Generally, the optical conductivity decreases with increasing the dopant content. In the higher range of light, the optical conductivity for all prepared samples exhibits an increasing trend of variation with increasing

incident photon energy. It is clear that the higher the range of light, the higher the optical conductivity values. This means that the prepared films can be used as ultraviolet photosensors and as optical receivers suitable for wireless light communications [88]. It is evident from Figure 4.16 that the optical conductivity decreased with increasing Fe content. The main reason lies beyond this decrease in the decreased carrier concentration (Table 4.5).

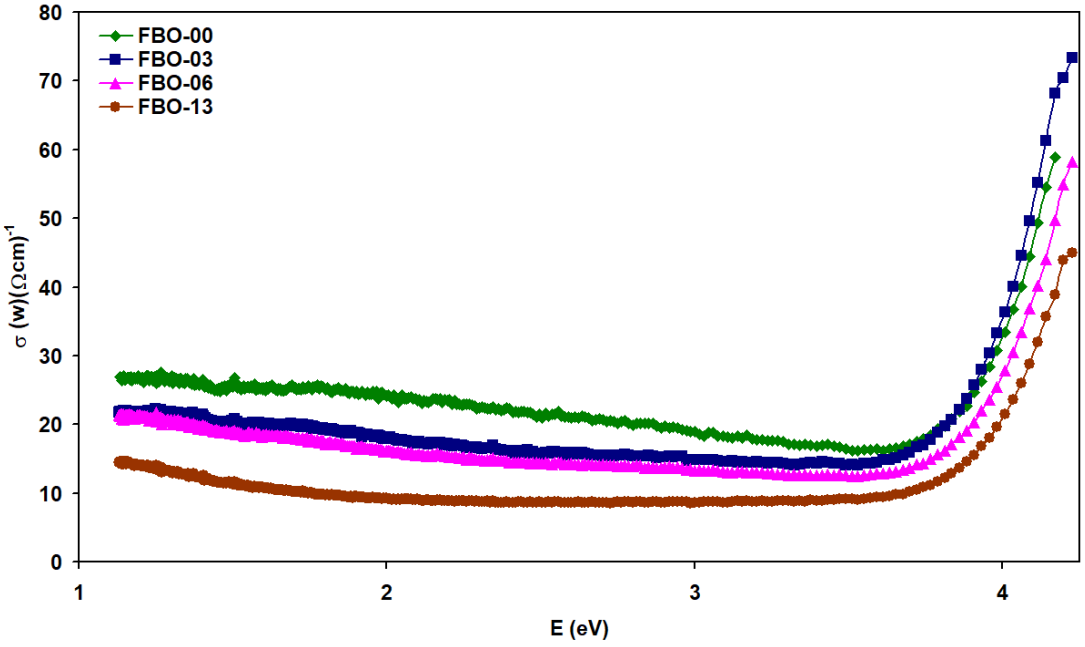

Figure 4.16. The optical conductivity spectra for the pure Bi_2O_3 and Fe-doped Bi_2O_3 samples.

On the other hand, the terahertz cutoff frequency spectra for all prepared samples, which are calculated from ($f_{co} = \frac{\sigma}{\varepsilon_r}$) are shown in Figure 4.17. The trend of variation of the terahertz cutoff frequency spectra contrasted with that of optical conductivity. In other words, the cutoff frequency increased with increasing doping content. The behavior of the cutoff frequency spectra depends on the optical conductivity to the dielectric constant values. Both parameters decreased with increasing Fe content. However, because the decrease in the dielectric constant is more pronounced than that

of the conductivity, the cutoff frequency increased. It is also noted that the values of the cutoff frequency are highly stable in a wide range of energies. This behavior can be regarded as an advantage because the stability of f_{co} means the performance of an optical device with the least noise effect and the possibility of a wide range of signal sources. The range can be extended from IR to visible light. These features are ideal for the fabrication of terahertz band filters.

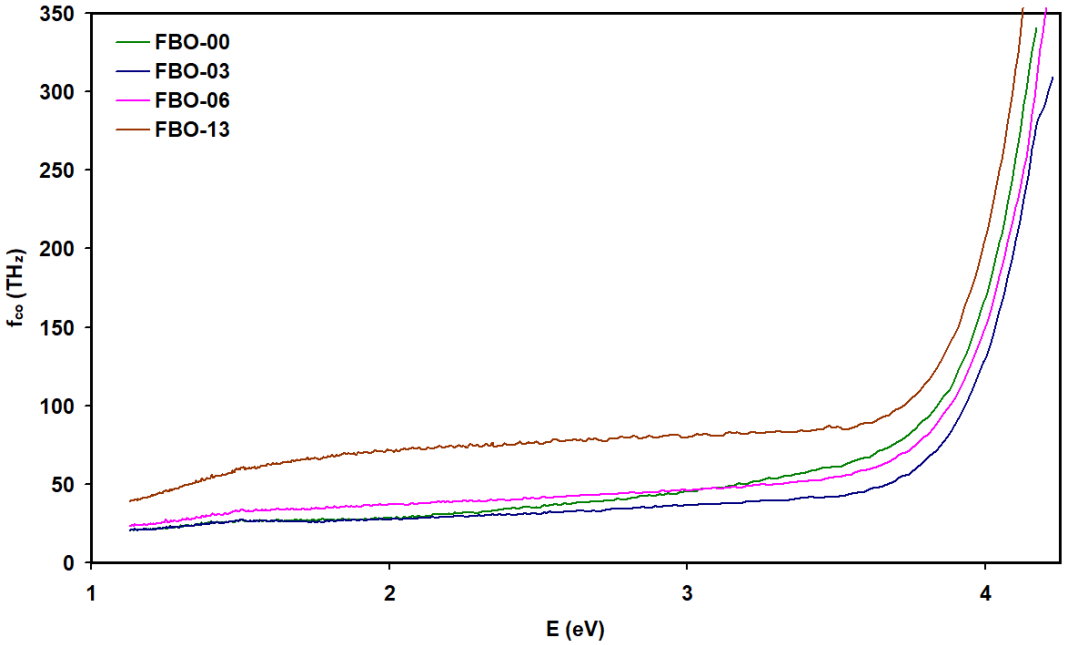

Figure 4.17. The terahertz cutoff frequency spectra for the pure Bi_2O_3 and Fe-doped Bi_2O_3 samples.

Chapter Five

Conclusions

In this study, we focused on studying the iron doping effects on the physical properties of bismuth oxide thin films. Three Fe doping contents were used for this purpose. The study considered the effect of doping on the structure and morphology of the films. The optical and dielectric properties were also considered. The analysis showed the preferred growth of the monoclinic structure of the films. The doping process affected the crystallinity by forming orthorhombic nanowire bundles of iron oxide in the bismuth oxide structure. This doping led to a decrease in the crystallite size and an increase in the micro-strain and defect density. The effect of the iron doping on the morphological properties of the films appeared through the appearance of grains with larger sizes and different shapes as the iron content increased. The appearance of nanowire bundles indicates that the solubility limit was exceeded, as also confirmed from the XRD measurements. The latter showed the existence of orthorhombic Fe_2O_3 in the samples doped with $13.0\ \mathrm{wt.\%}$ Fe. The optical analysis showed that the iron doping reduced the band gap energy, the dielectric constant, the optical conductivity and enhanced the terahertz cutoff frequency. Even though, the dielectric constant values remained high. The high values of the dielectric constant are suitable for field effect transistor technology. In addition, the stability of the terahertz cutoff frequency in a wide range of energy is adequate for enhanced performance of optical devices, such as band filters. On the other hand, the modeling of the dielectric constant via the Drude-Lorentz approach allowed determining the optical conductivity parameters, which indicated that the electron concentrations as well as the Plasmon frequency decreased

with increasing doping content. The parameters are promising for using the pure and Fe-doped Bi_2O_3 samples in sensing applications.

References

Sosna-Głębska, A., Szczecińska, N., Znajdek, K., & Sibiński, M. (2019). Review on metallic oxide nanoparticles and their application in optoelectronic devices. *Acta Innovations*, (30), 5-15.

Yu, X., Marks, T. J., & Facchetti, A. (2016). Metal oxides for optoelectronic applications. *Nature materials*, *15*(4), 383-396.

Pérez-Tomás, A., Mingorance, A., Tanenbaum, D., & Lira-Cantú, M. (2018). Metal oxides in photovoltaics: all-oxide, ferroic, and perovskite solar cells. In *The future of semiconductor oxides in next-generation solar cells* (pp. 267-356). Elsevier.

Gerling, L. G., Mahato, S., Morales-Vilches, A., Masmitja, G., Ortega, P., Voz, C., Alcubilla, R., & Puigdollers, J. (2016). Transition metal oxides as hole-selective contacts in silicon heterojunctions solar cells. *Solar Energy Materials and Solar Cells*, *145*, 109-115.

Nunes, D., Pimentel, A., Gonçalves, A., Pereira, S., Branquinho, R., Barquinha, P., Fortunato, E., & Martins, R. (2019). Metal oxide nanostructures for sensor applications. *Semiconductor Science and Technology*, *34*(4), 043001.

Khan, M. M., Adil, S. F., & Al-Mayouf, A. (2015). Metal oxides as photocatalysts. *Journal of Saudi chemical society*, *19*(5), 462-464.

Vasanthi, V., Sivanantham, N., Saathvika, L., & Gopalakrishnan, N. (2023). Metal oxide charge transport materials for light emitting diodes-An overview. *Materials Science in Semiconductor Processing*, *165*, 107679.

Liang, R., Du, Y., Xiao, P., Cheng, J., Yuan, S., Chen, Y., Yuan, J., & Chen, J. (2021). Transition metal oxide electrode materials for supercapacitors: a review of recent developments. *Nanomaterials*, *11*(5), 1248.

Bredar, A. R., Chown, A. L., Burton, A. R., & Farnum, B. H. (2020). Electrochemical impedance spectroscopy of metal oxide electrodes for energy applications. *ACS Applied Energy Materials*, *3*(1), 66-98.

Qasrawi, A. F., & Daragme, R. B. (2022). Yb/Se/WO3/Yb Thin Film Transistors as Rectifiers, N-Channel Metal Oxide Semiconductor Capacitors, Laser Sensors, and Microwave Bandstop Filters. *physica status solidi (a)*, *219*(18), 2100822.

Gong, Y., Zhang, S., Gao, H., Ma, Z., Hu, S., & Tan, Z. A. (2020). Recent advances and comprehensive insights on nickel oxide in emerging optoelectronic devices. *Sustainable energy & fuels*, *4*(9), 4415-4458.

Zhao, Z., Tian, J., Sang, Y., Cabot, A., & Liu, H. (2015). Structure, synthesis, and applications of TiO2 nanobelts. *Advanced materials*, *27*(16), 2557-2582.

Mirzaeian, M., Ogwu, A. A., Jirandehi, H. F., Aidarova, S., Ospanova, Z., & Tsendzughul, N. (2017). Surface characteristics of silver oxide thin film electrodes for supercapacitor applications. *Colloids and Surfaces A: Physicochemical and Engineering Aspects*, *519*, 223-230.

Dalapati, G. K., Sharma, H., Guchhait, A., Chakrabarty, N., Bamola, P., Liu, Q., Saianand, G., Krishna, A.M.S., Mukhopadhyay, S., Dey, A & Sharma, M. (2021). Tin oxide for optoelectronic, photovoltaic and energy storage devices: a review. *Journal of materials chemistry A*, *9*(31), 16621-16684.

Kour, S., Sharma, R. K., Jasrotia, R., & Singh, V. P. (2019, August). A brief review on the synthesis of maghemite (γ-Fe2O3) for medical diagnostic and solar energy applications. In *AIP Conference Proceedings* (Vol. 2142, No. 1). AIP Publishing.

Lv, X., Li, Z., Zhang, J., & Yang, B. (2015). A facile approach to prepare bismuth oxide nanorods for application in optoelectronic devices. *Chemistry Letters*, *44*(1), 97-99.

Gadhi, T. A., Hernández-Gordillo, A., Bizarro, M., Jagdale, P., Tagliaferro, A., & Rodil, S. E. (2016). Efficient α/β-Bi2O3 composite for the sequential photodegradation of two-dyes mixture. *Ceramics International*, *42*(11), 13065-13073.

Xu, H., Hu, X., Yang, H., Sun, Y., Hu, C., & Huang, Y. (2015). Flexible asymmetric micro-supercapacitors based on Bi2O3 and MnO2 nanoflowers: larger areal mass promises higher energy density. *Advanced Energy Materials*, *5*(6), 1401882.

Chen, R., Hu, W., Zou, L., Li, B., & Bao, D. (2015). Highly uniform resistive switching effect in amorphous Bi 2 O 3 thin films fabricated by a low-temperature photochemical solution deposition method. *Applied Physics A*, *120*, 379-384.

Khusayfan, N. M., Qasrawi, A. F., & Khanfar, H. K. (2017). Impact of Yb, In, Ag and Au thin film substrates on the crystalline nature, Schottky barrier formation and microwave trapping properties of Bi2O3 films. *Materials Science in Semiconductor Processing*, *64*, 63-70.

Sindhu, S. (2015). α-Bi 2 O 3 photoanode in DSSC and study of the electrode–electrolyte interface. *RSC advances*, *5*(95), 78299-78305.

Iyyapushpam, S., Nishanthi, S. T., & Padiyan, D. P. (2015). Synthesis of β-Bi2O3 towards the application of photocatalytic degradation of methyl orange and its instability. *Journal of Physics and Chemistry of Solids*, *81*, 74-78.

Matysiak, W. (2022). Synthesis of 1D Bi2O3 nanostructures from hybrid electrospun fibrous mats and their morphology, structure, optical and electrical properties. *Scientific Reports*, *12*(1), 4046.

Sharma, R., Khanuja, M., Sharma, S. N., & Sinha, O. P. (2017). Reduced band gap & charge recombination rate in Se doped α-Bi2O3 leads to enhanced photoelectrochemical and photocatalytic performance: theoretical & experimental insight. *international journal of hydrogen energy*, *42*(32), 20638-20648.

Navaneeth, A., & Sindhu, S. (2015). Improved carrier mobility and bandgap tuning of zinc doped bismuth oxide. *RSC Advances*, *5*(4), 2504-2510.

Liu, X., Deng, H., Yao, W., Jiang, Q., & Shen, J. (2015). Preparation and photocatalytic activity of Y-doped Bi2O3. *Journal of Alloys and Compounds*, *651*, 135-142.

Bilgin, V., Sarica, E., Demirselcuk, B., & Turkyilmaz, S. (2018). Iron doped ZnO thin films deposited by ultrasonic spray pyrolysis: structural, morphological, optical, electrical and magnetic investigations. *Journal of Materials Science: Materials in Electronics*, *29*, 17542-17551.

Viveka, S. S., Logu, T., Ahsan, N., Karthikeyan, J., Murugan, P., Sampath, M., Kalainathan, S., Gupta, A., Okada, Y., & Sethuraman, K. (2021). Fe-doped CuGaS2 (CuGa1-xFexS2)-Detailed analysis of the intermediate band optical response of chalcopyrite thin films based on first principle calculations and experimental studies. *Materials Science in Semiconductor Processing*, *136*, 106133.

Rajeswari, S., Ibrahim, M. M., Raj, I. L. P., Hakami, J., Imran, M., AlFaify, S., & Shkir, M. (2022). Noticeably enhanced photosensing properties of Fe-doped Bi2S3 thin films developed by nebulizer spray pyrolysis technique for photosensor applications. *Sensors and Actuators A: Physical*, *345*, 113759.

Xiaohong, W., Wei, Q., Li, L., Yun, G., & Zhaoyang, X. (2009). Photocatalytic property of nanostructured Fe3+-doped Bi2O3 films. *Catalysis Communications*, *10*(5), 600-604.

Neamen, D. (2002). *Semiconductor physics and devices*. Third Edition, New York: McGraw-Hill higher education.

Yamaki, T., Umebayashi, T., Sumita, T., Yamamoto, S., Maekawa, M., Kawasuso, A., & Itoh, H. (2003). Fluorine-doping in titanium dioxide by ion implantation technique. *Nuclear Instruments and Methods in Physics Research Section B: Beam Interactions with Materials and Atoms*, *206*, 254-258.

Ito, Y., Christodoulou, C., Nardi, M. V., Koch, N., Sachdev, H., & Mullen, K. (2014). Chemical vapor deposition of N-doped graphene and carbon films: the role of precursors and gas phase. *ACS nano*, *8*(4), 3337-3346.

Sheeba, N. H., Vattappalam, S. C., Naduvath, J., Sreenivasan, P. V., Mathew, S., & Philip, R. R. (2015). Effect of Sn doping on properties of transparent ZnO thin films prepared by thermal evaporation technique. *Chemical Physics Letters*, *635*, 290-294.

Mahroug, A., Boudjadar, S., Hamrit, S., & Guerbous, L. (2014). Structural, optical and photocurrent properties of undoped and Al-doped ZnO thin films deposited by sol–gel spin coating technique. *Materials Letters*, *134*, 248-251.

Suja, M., Bashar, S. B., Morshed, M. M., & Liu, J. (2015). Realization of Cu-doped p-type ZnO thin films by molecular beam epitaxy. *ACS Applied materials & interfaces*, *7*(16), 8894-8899.

Omareya, O. A., Qasrawi, A. F., & Al Garni, S. E. (2017). Effect of Au nanosandwiching on the structural, optical and dielectric properties of the as grown and annealed InSe thin films. *Physica B: Condensed Matter*, *520*, 57-64.

Alfhaid, L. H. K., Qasrawi, A. F., & Khanfar, H. K. (2023). Characterization of PbWO4 thin films formed by the pulsed laser welding technique. *Materials Today Communications*, *35*, 106157.

Ali, A., Chiang, Y. W., & Santos, R. M. (2022). X-ray diffraction techniques for mineral characterization: A review for engineers of the fundamentals, applications, and research directions. *Minerals*, *12*(2), 205.

Falsafi, S. R., Rostamabadi, H., & Jafari, S. M. (2020). X-ray diffraction (XRD) of nanoencapsulated food ingredients. In *Characterization of nanoencapsulated food ingredients* (pp. 271-293). Academic press.

Dinnebier, R. E., & Billinge, S. J. L. (2019). The Bragg equation derived. *International Tables for Crystallography 2019. H. ch. 1.1* , 2-4.

Muniz, F. T. L., Miranda, M. R., Morilla dos Santos, C., & Sasaki, J. M. (2016). The Scherrer equation and the dynamical theory of X-ray diffraction. *Acta Crystallographica Section A: Foundations and Advances*, *72*(3), 385-390.

He, K., Chen, N., Wang, C., Wei, L., & Chen, J. (2018). Method for determining crystal grain size by x-ray diffraction. *Crystal Research and Technology*, *53*(2), 1700157.

Monshi, A., Foroughi, M. R., & Monshi, M. R. (2012). Modified Scherrer equation to estimate more accurately nano-crystallite size using XRD. *World journal of nano science and engineering*, *2*(3), 154-160.

Akl, A. S., & Elhadi, M. (2020). Estimation of crystallite size, lattice parameter, internal strain and crystal impurification of nanocrystalline Al3Ni20Bx alloy by Williamson-Hall method. *Journal of Ovonic Research Vol*, *16*(5), 323-335.

Alharbi, S. R., & Qasrawi, A. F. (2021). Effects of Au nanoslabs on the performance of CdO thin films designed for optoelectronic applications. *Physica E: Low-dimensional Systems and Nanostructures*, *125*, 114386.

Kumar, S., & Das, B. (2017). Effect of lattice strain on X-ray Diffraction, Raman Spectroscopy and Optical Properties of as Synthesis Nanocomposite ZnO-SnO2—TiO2 Thin Film by Spray Pyrolysis Method. *Semant. Sch*, *2017*, 5204639.

Ameh, E. S. (2019). A review of basic crystallography and x-ray diffraction applications. *The international journal of advanced manufacturing technology*, *105*(7), 3289-3302.

Kittel, C., & McEuen, P. (2018). *Introduction to solid state physics*. Eighth edition, Hoboken: John Wiley & Sons.

Fox, M. (2002). Optical properties of solids. New York: Oxford university press.

Makuła, P., Pacia, M., & Macyk, W. (2018). How to correctly determine the band gap energy of modified semiconductor photocatalysts based on UV–Vis spectra. *The journal of physical chemistry letters*, *9*(23), 6814-6817.

Asmat Uceda, M. A. (2010). Synthesis and characterization of delafossite thin films by reactive RF magnetron sputtering. *Ph. D. Thesis*.

He, T., Ehrhart, P., & Meuffels, P. (1996). Optical band gap and Urbach tail in Y-doped BaCeO3. *Journal of applied physics*, *79*(6), 3219-3223.

Rai, R. C. (2013). Analysis of the Urbach tails in absorption spectra of undoped ZnO thin films. *Journal of Applied Physics*, *113*(15).

Dresselhaus, M., Dresselhaus, G., Cronin, S. B., & Souza Filho, A. G. (2018). Solid State Properties. *Alemania: Springer-Verlag*.

Sokolik, I., Andronova, A., & Johnson, T. C. (1993). Complex refractive index of atmospheric dust aerosols. *Atmospheric Environment. Part A. General Topics*, *27*(16), 2495-2502.

Cheng, H., Huang, B., Lu, J., Wang, Z., Xu, B., Qin, X., Zhang, X. & Dai, Y. (2010). Synergistic effect of crystal and electronic structures on the visible-light-driven photocatalytic performances of Bi2O3 polymorphs. *Physical Chemistry Chemical Physics*, *12*(47), 15468-15475.

Qasrawi, A. F., & Zyoud, H. M. (2020). Dielectric dispersion at the Mn/ZnPc interfaces. *physica status solidi (b)*, *257*(6), 2000089.

Qasrawi, A. F., & Aloushi, H. D. (2019). In situ monitoring of the permanent crystallization, phase transformations and the associated optical and electrical enhancements upon heating of Se thin films. *Physica B: Condensed Matter*, *569*, 62-67.

Hamed, M. H., Mueller, D. N., & Müller, M. (2020). Thermal phase design of ultrathin magnetic iron oxide films: from Fe 3 O 4 to γ-Fe 2 O 3 and FeO. *Journal of Materials Chemistry C*, *8*(4), 1335-1343.

Tuček, J., Machala, L., Ono, S., Namai, A., Yoshikiyo, M., Imoto, K., ... & Zbořil, R. (2015). Zeta-Fe2O3–A new stable polymorph in iron (III) oxide family. *Scientific reports*, *5*(1), 15091.

Qasrawi, A. F., Sahin, E. İ., Abed, T. Y., & Emek, M. (2021). Structural and dielectric properties of Ba1− xLax (Zn1/3Nb2/3) O3 solid solutions. *physica status solidi (b)*, *258*(3), 2000419.

Debnath, S., Deb, K., Saha, B., & Das, R. (2019). X-ray diffraction analysis for the determination of elastic properties of zinc-doped manganese spinel ferrite nanocrystals (Mn0. 75Zn0. 25Fe2O4), along with the determination of ionic radii, bond lengths, and hopping lengths. *Journal of Physics and Chemistry of Solids*, *134*, 105-114.

Prabakar, C., Muthukumaran, S., & Raja, V. (2020). Structural, magnetic and photoluminescence behavior of Ni/Fe doped ZnO nanostructures prepared by co-precipitation method. *Optik*, *202*, 163714.

Kou, G., Mu, M., Lin, M., Zhu, Z., Yang, X., & Yang, Y. (2023). Enhancing multi-state programming and synaptic plasticity through optical stimulation in Bi-alloyed Cs2AgInCl6 double perovskite based memristor. *Journal of Alloys and Compounds*, *957*, 169999.

Alharbi, S. R., & Qasrawi, A. F. (2019). Effects of Ge substrate on the structural and optical conductivity parameters of Bi2O3 thin films. *Optik*, *181*, 714-720.

Lu, C., Amsler, M., & Chen, C. (2018). Unraveling the structure and bonding evolution of the newly discovered iron oxide FeO2. *Physical Review B*, *98*(5), 054102.

Qin, W., Qi, J., & Wu, X. (2014). Photocatalytic property of Cu2+-doped Bi2O3 films under visible light prepared by the sol–gel method. *Vacuum*, *107*, 204-207.

Krishna Reddy, J., Srinivas, B., Durga Kumari, V., & Subrahmanyam, M. (2009). Sm3+-doped Bi2O3 photocatalyst prepared by hydrothermal synthesis. *ChemCatChem*, *1*(4), 492-496.

Lowes, W., & Liu, J. (2011). Synthesis and Characterization of ZnO/α-Fe2O3 Nano-Architectures. *Microscopy and Microanalysis*, *17*(S2), 1726-1727.

Pandiadurai, K., Mani, G. K., Shankar, P., & Rayappan, J. B. B. (2013). ZnO nanospheres to nanorods–morphology transition via Fe-doping. *Superlattices and Microstructures*, *62*, 39-46.

Hajakbari, F., & Ensandoust, M. (2016). Study of thermal annealing effect on the properties of silver thin films prepared by DC magnetron sputtering. *Acta Physica Polonica A*, *129*(4), 680-682.

Norouzzadeh, P., Mabhouti, K., Golzan, M. M., & Naderali, R. (2020). Investigation of structural, morphological and optical characteristics of Mn substituted Al-doped ZnO NPs: a Urbach energy and Kramers-Kronig study. *Optik*, *204*, 164227.

Qasrawi, A. F. (2019). Effect of Y, Au and YAu nanosandwiching on the structural, optical and dielectric properties of ZnSe thin films. *Chalcogenide Letters*, 16(3), 95-105.

Al Garni, S. E., & Qasrawi, A. F. (2018). Characterization of Bi2O3/ZnS heterojunctions designed for visible light communications. *Materials Research Express*, *6*(3), 036205.

Sha, T., Li, W., Chen, S., Jiang, K., Zhu, J., Hu, Z., Huang, Z., Chu, J., Kokh, K.A., & Andreev, Y. M. (2017). Effects of S-doping on the electronic transition, band gap, and optical absorption of GaSe1− xSx single crystals. *Journal of Alloys and Compounds*, *721*, 164-171.

Baqiah, H., Talib, Z. A., Liew, J. Y. C., Shaari, A. H., Zainal, Z., & Laimy, M. F. (2020). Effects of precursor concentration on the microstructural, optical and photoelectrochemical properties of Bi2O3 films synthesized by sol-gel method. *Optik*, *206*, 164303.

Durgam, K., Eppa, R., & MV, R. R. (2021). Effect of metal ions doping on structural, optical properties and photocatalytic activity of anatase TiO2 thin films. *Surface and Interface Analysis*, *53*(2), 194-205.

Kamarulzaman, N., Kasim, M. F., & Rusdi, R. (2015). Band gap narrowing and widening of ZnO nanostructures and doped materials. *Nanoscale research letters*, *10*, 1-12.

Akshay, V. R., Arun, B., Mandal, G., Chanda, A., & Vasundhara, M. (2019). Significant reduction in the optical band-gap and defect assisted magnetic response in Fe-doped anatase TiO 2 nanocrystals as dilute magnetic semiconductors. *New Journal of* Chemistry, *43*(15), 6048-6062.

Saleh, R., Prakoso, S. P., & Fishli, A. (2012). The influence of Fe doping on the structural, magnetic and optical properties of nanocrystalline ZnO particles. *Journal of Magnetism and Magnetic Materials*, *324*(5), 665-670.

Huang, Y., Qin, J., Hu, C., Liu, X., Wei, D., & Seo, H. J. (2019). Cs-doped α-Bi2O3 microplates: hydrothermal synthesis and improved photochemical activities. *Applied Surface Science*, *473*, 401-408.

Wei, X., Wen, J., Li, S., Huang, S., Cheng, J., Chen, Y., Duan, C., & Yin, M. (2014). Red-shift of vanadate band-gap by cation substitution for application in phosphor-converted white light-emitting diodes. *Applied Physics Letters*, *104*(18), 181904.

Qasrawi, A. F., & Gasanly, N. M. (2013). Mixed conduction and anisotropic single oscillator parameters in low dimensional TlInSe2 crystals. *Materials Chemistry and Physics*, *141*(1), 63-68.

Al Garni, S. E., Omareye, O. A., & Qasrawi, A. F. (2017). Growth and characterization of InSe/Ge/InSe interfaces. *Optik*, *144*, 340-347.

Jiang, S., Wang, L., Hao, W., Li, W., Xin, H., Wang, W., & Wang, T. (2015). Visible-light photocatalytic activity of S-doped α-Bi2O3. *The Journal of Physical Chemistry C*, *119*(25), 14094-14101.

Li, S. Á., Haller, E. Á., Yu, K. Á., Walukiewicz, W., Ager, J. W., Wu, J., Shan, W., Lu, H.,& Schaff, W. J. (2005). Effect of native defects on optical properties of InxGa1− xN alloys. *Applied Physics Letters*, *87*(16),161905.

Qasrawi, A. F., & Imair, S. N. (2022). Enhanced structural, optical and dielectric properties of the Se/CdBr2 interfaces designed as terahertz optical receivers. *Optical and Quantum Electronics*, *54*(11), 746.

الملخص

لقد ناقشنا في هذه الأطروحة تأثير تطعيم الحديد على الخواص الهيكلية والشكلية والتركيبية والبصرية والعازلة للأغشية الرقيقة لأكسيد البزموث. تم ترسيب أغشية رقيقة من أكسيد البزموث بسماكة 0.50 ميكرومتر عن طريق التبخير الحراري لمساحيق أكسيد البزموث على ركائز زجاجية تحت ضغط تفريغ قدره تقريبا 10^{-4} ملي بار. تم تطعيم الرقائق بالحديد من خلال خلط مساحيق الحديد النانوية مع مساحيق أكسيد البزموث قبل التبخير. تم استخدام ثلاثة كميات متزايدة من الحديد لهذا الغرض. وقد لوحظ أن الأغشية المحضرة تكون متعددة البلورات بطبيعتها وأن عملية التطعيم أدت الى نقصان في حجم البلورات وزيادة في التلف المايكروي وكثافة العيوب. أظهر المجهر الإلكتروني الماسح حبيبات بأحجام متزايدة وأشكال مختلفة حسب كمية الحديد المطعمة. بصريًا، أظهرت الرقائق المطعمة قيم نفاذية منخفضة وأظهرت انخفاضا في فجوة نطاق الطاقة مع زيادة محتوى الحديد. من ناحية أخرى، أظهرت تحليلات تشتت العزل الكهربائي تحسن استجابة ثابت العزل بما يتناسب مع العوازل المستخدمة في تكنولوجيا الترانزستور ذو الأغشية الرقيقة والتي تعتمد في عملها على البوابات ذات ثابت عازليه مرتفع. تم تحليل ثابت العزل التخيلي باستخدام نموذج Drude-Lorentz الذي يربط المعلومات الكهربائية بتلك البصرية ومقارنتها بالبيانات التجريبية التي وضحت نقصان كثافة الالكترونات مع زيادة محتوى الحديد في أكسيد البزموث. يعتبر هذا العمل واعدًا لأنه يعزز أداء أكسيد البزموث ويجعله مناسبًا للتطبيقات الإلكترونية.